A&A 541, A118 (2012)
DOI: 10.1051/0004-6361/201117314

Astronomy & Astrophysics

AGN-host galaxy connection: morphology and colours of X-ray selected AGN at $z \leq 2^{\star}$

M. Pović[1,2,3], M. Sánchez-Portal[4,5], A. M. Pérez García[1,6,5], A. Bongiovanni[1,6,5], J. Cepa[5,1], M. Huertas-Company[7,8], M. A. Lara-López[1,9], M. Fernández Lorenzo[1,3], A. Ederoclite[1,10], E. Alfaro[3], H. Castañeda[11], J. Gallego[12], J. I. González-Serrano[13], and J. J. González[14]

[1] Instituto de Astrofísica de Canarias (IAC), La Laguna, Tenerife, Spain
e-mail: mpovic@iaa.es
[2] Astrophysics and Cosmology Research Unit (ACRU), School of Mathematical Sciences, University of Kwa-Zulu Natal (UKZN), Durban, South Africa
[3] Instituto de Astrofísica de Andalucía (IAA-CSIC), Granada, Spain
[4] Herschel Science Centre (HSC), European Space Agency Centre (ESAC)/INSA, Villanueva de la Cañada, Madrid, Spain
e-mail: miguel.sanchez@sciops.esa.int
[5] Asociación ASPID, Apartado de Correos 412, La Laguna, Tenerife, Spain
[6] Departamento de Astrofísica, Universidad de La Laguna (ULL), La Laguna, Tenerife, Spain
[7] GEPI, Paris-Meudon Observatory, Meudon, France
[8] University of Paris, Paris, France
[9] Australian Astronomical Observatory, PO Box 296, Epping NSW 1710, Australia
[10] Centro de Estudios de Física del Cosmos de Aragón (CEFCA), Teruel, Spain
[11] Escuela Superior de Física y Matemáticas, Intituto Politécnico Nacional (IPN), Mexico D.F., Mexico
[12] Departamento de Astrofísica y CC. de la Atmósfera, Universidad Complutense de Madrid, Madrid, Spain
[13] Instituto de Física de Cantabria, CSIC-Universidad de Cantabria, Santander, Spain
[14] Instituto de Astronomía UNAM, México D.F., México

Received 22 May 2011 / Accepted 3 February 2012

ABSTRACT

Context. The connection between active galactic nuclei (AGN) and their host galaxies has been widely studied and found to be of great importance for providing answers to some fundamental questions related to AGN fuelling mechanisms, and both their formation and evolution.

Aims. Using X-ray data and one of the deepest broad-band optical data sets available, we study how morphology and colours are related to X-ray properties for sources at redshifts $z \leq 2.0$, using a sample of 262 AGN in the Subaru/*XMM-Newton* Deep Survey (SXDS).

Methods. We performed our morphological classification using the galSVM code, which is a new method that is particularly suited to dealing with high-redshift sources. Colour–magnitude diagrams were studied in relationship to redshift, morphology, X-ray obscuration, and X-ray-to-optical flux ratio. We analysed the different regions in the colour–magnitude diagrams, and searched for correlations with the observed properties of AGN populations using models of their formation and evolution.

Results. We confirm that a robust and reliable morphological classification of a general galaxy population at high redshift should be based on a multi-parametric approach. At least 50% of X-ray detected AGN at $z \leq 2.0$ analysed in this work reside in spheroidal and bulge-dominated galaxies, while at least 18% have disk-dominated hosts. This suggests that different mechanisms may be responsible for triggering the nuclear activity. When analysing populations of X-ray detected AGN in both colour–magnitude and colour-stellar mass diagrams, the highest number of sources is found to reside in the green valley at redshifts ≈0.5–1.5. However, a larger number of low-luminosity AGN have been detected than in previous works owing to the substantial depth of the SXDS optical data. Whether AGN are hosted by early- or late-type galaxies, no clear relationship has been found with the optical colours (independently of redshift), as is typical of normal galaxies. Both early- and late-type AGN cover similar ranges of X-ray obscuration, for both unobscured and obscured sources.

Conclusions. Our findings appear to confirm some previous suggestions that X-ray selected AGN residing in the green valley represent a transitional population, quenching star formation by means of different AGN feedback mechanisms and evolving to red-sequence galaxies. They might be hosted by similar sources (the majority of sources being late-type elliptical and lenticular galaxies, and early-type spirals) with similar stellar populations, which are triggered mainly by major and/or minor mergers, and in some cases by means of secular mechanism, as shown in previous numerical simulations. In the aforementioned transition we observe different phases of AGN activity, with some AGN being in the "QSO-mode" detected as compact, blue, and unobscured in X-rays, and with others passing through different phases before and after the "QSO-mode", being obscured and unobscured in X-rays, respectively.

Key words. galaxies: active – galaxies: fundamental parameters – galaxies: distances and redshifts – galaxies: structure – X-rays: galaxies

1. Introduction

Active galactic nuclei (AGN) play an important role in many aspects of modern cosmology, and are of particular interest to

⋆ Full Table A.1 is only available at the CDS via anonymous ftp to cdsarc.u-strasbg.fr (130.79.128.5) or via http://cdsarc.u-strasbg.fr/viz-bin/qcat?J/A+A/541/A118

the interplay between AGN and their host galaxies. The study of AGN host galaxies is shown to be of great importance for providing answers to some still unanswered questions. These questions include what is (1) the effect of the AGN on their host galaxy and vice-versa, (2) the origin of the accretion material, (3) the triggering mechanisms that initiate the active phase in a galaxy, and (4) the duration of the active phase, therefore placing important constraints on the models of supermassive black hole (SMBH) formation and growth, as well as the formation and evolution of galaxies.

Over recent years, fundamental relationships between the AGN and host galaxy properties have been found, particularly for the galaxy bulges, which provide evidence of a connection between galaxy formation and AGN activity. This involves the discoveries that most of the close massive galaxies have a SMBH at their centres (Magorrian et al. 1998), that local AGN predominantly reside in galaxies dominated by a massive bulge (Kauffmann et al. 2003), and that the masses of the central SMBHs in nearby galaxies correlate with several host bulge properties, including luminosity (Kormendy & Richstone 1995; McLure et al. 2000; Marconi & Hunt 2003), velocity dispersion (Ferrarese & Merritt 2000; Gebhardt et al. 2000), mass (Magorrian et al. 1998; Ferrarese 2004), and galaxy light concentration (Graham et al. 2001a). Moreover, across a wide range of redshifts it has been found that early-type galaxies, which have more massive black holes at their centres, have lower Eddington ratios than later-type galaxies (Hickox et al. 2009; Pović et al. 2009a,b).

Morphology and colours are two key elements used to study the properties of AGN host galaxies, their connection with AGN, and their evolution. They represent two of the most accessible indicators of the galaxy's physical structure, being crucial to understanding the formation of galaxies throughout cosmic history and providing answers to some of the fundamental questions mentioned above.

The morphological study of AGN host galaxies has been an active research field in the past few years, which has revealed an inconsistency between the results obtained for samples at both low and high redshifts, with different methods of morphological classification. The first important morphological study of local AGN (mostly Seyfert galaxies) showed that most of them reside in spiral galaxies (e.g., Adams 1977; Heckman 1978; Ho et al. 1995). However, Kauffmann et al. (2003) analysed thousands of low-redshift ($z \leq 0.4$) AGN host galaxies from the Sloan Digital Sky Survey (SDSS), and found that most AGN reside in massive galaxies, whose distributions of sizes, stellar surfaces, mass densities, and concentrations, all reseamble those of early-type SDSS galaxies. On the other hand, Choi et al. (2009) found that most AGN from the SDSS survey reside in late-type galaxies with intermediate luminosities and velocity dispersions. Deep surveys made it possible to study the morphological properties of intermediate- and high-redshift AGN host galaxies selected at different wavelengths (mainly X-ray, optical, infrared (IR), and radio). Most of these studies found that X-ray selected AGN usually reside in spheroid/bulge-dominated galaxies (e.g., Pierce et al. 2007; Pović et al. 2009a), although some studies found a higher concentrations of later-types (Gabor et al. 2009).

Besides morphology, colours are also important for revealing the nature of AGN host galaxies. It is well-known from previous studies of colour–magnitude relations that, in general, normal galaxies may be located in the "red sequence", populated by massive, bulge-dominated galaxies with older, passively evolving stellar populations, or in the "blue cloud", populated by blue, star-forming galaxies of small and intermediate masses (e.g., Baldry et al. 2004; Weiner et al. 2005; Cirasuolo et al. 2005). In most (if not all) studies, galaxies hosting AGN lie predominantly in the "green valley" of the colour–magnitude diagrams, a transition region located between the red sequence and the blue cloud (e.g., Barger et al. 2003; Sánchez et al. 2004; Nandra et al. 2007; Georgakakis et al. 2008; Silverman et al. 2008; Treister et al. 2009). This has been considered as one of the pieces of evidence of a connection between AGN and galaxy evolution, suggesting that the AGN feedback mechanism may play an important role in regulating (quenching) star formation, moving the galaxies from blue, star-forming to passive, red-sequence galaxies (e.g., Springel et al. 2005; Schawinski et al. 2006; Hasinger 2008). Hickox et al. (2009) studied three populations of AGN, selected in radio, X-ray, and IR, and found that most radio-selected AGN are hosted by red-sequence galaxies, that X-ray selected AGN occupy all areas of the colour–magnitude diagram, but mostly the green valley, while most IR-selected AGN reside in slightly bluer galaxies than the two previous populations. However, other results show that there is no strong evidence in AGN host galaxies of either highly suppressed star formation, which is expected if AGN are responsible for star-formation quenching, or elevated star formation, when compared to galaxies of similar stellar masses and redshifts (Alonso-Herrero et al. 2008; Brusa et al. 2009).

As mentioned above, although many analyses have been carried out over the past few years to study the morphological and colour properties of AGN host galaxies, there are still many inconsistencies between the results obtained and their interpretation. In particular, the interpretation of morphology still remains a problem in the framework of galaxy evolution. Since the quality of the measured morphology is depends strongly on the image resolution, the morphological classification in deep surveys remains very difficult, especially when dealing with faint and high redshift sources. Therefore, additional studies are necessary using deep observations to obtain large samples of AGN and test new methods of morphological classification, to reveal the nature of AGN host galaxies and their connection with AGN, and to study their evolution throughout cosmic time.

In this work, we perform a study of the morphological and colour properties of a sample of 262 X-ray detected AGN at redshifts $z \leq 2$ in the Subaru/*XMM-Newton* Deep Survey (SXDS; Furusawa et al. 2008) field, using one of the deepest optical datasets available to the astronomical community. Morphological classification was performed using galSVM (Huertas-Company et al. 2008, 2009), one of a new codes that is especially useful for analysing morphology when dealing with low spatial resolution and high redshift data. A set of different morphological parameters have been studied, and an additional visual classification has been performed. The evolution of the AGN host galaxies on the colour–magnitude diagrams has been studied in four redshift intervals (up to $z \leq 2$ in bins of 0.5), for different morphological and X-ray types, and for objects with different X-ray-to-optical (X/O) flux ratios. Different regions of the colour–magnitude diagrams have been analysed, relating the observed AGN properties in each region to some current models of AGN formation and evolution. Finally, this paper provides the scientific community with a catalogue of a large sample of AGN detected in the SXDS field, including their photometric X-ray and optical data, morphological properties, rest-frame colours, and redshifts. The catalogue can be used in further studies related to AGN populations. This paper is part of the preparatory work for the long-term OTELO[1] survey (Cepa et al. 2008),

[1] OSIRIS Tunable Emission Line Object survey.

which is an on-going emission-line survey using the tunable filters of OSIRIS[2] at the GTC[3] telescope. The survey aims to perfom a narrow-band tomography over a 21 nm window centred at 920 nm in at least two selected fields, and its science cases include the study of the SFR density and chemical evolution in the Universe, high redshift QSO and AGN at any redshift, emission-line ellipticals, and Galactic emission-line stars (Cepa et al. 2007; Pović et al. 2009a; Lara-López et al. 2010; Cepa et al. 2011).

The paper is structured as follows: in Sect. 2, we describe the observational data used in this work, including a brief summary of the X-ray data processing and source detection, optical broad-band data, selection of X-ray emitters with optical counterparts, and estimation of the k-corrections and photometric redshifts. Section 3 describes the morphological classification of X-ray selected AGN. All analysis related to AGN colours is described in Sect. 4, where it is considered in relation to redshift, morphology, X-ray obscuration, and X/O flux ratio, by comparing the obtained results with some models of AGN formation and evolution. Finally, Sect. 5 summarises the main results obtained in this work. The concordance cosmology with $\Omega_\Lambda = 0.7$, $\Omega_M = 0.3$, and $H_0 = 70\,\mathrm{km\,s^{-1}\,Mpc^{-1}}$ is assumed. Unless otherwise specified, all magnitudes are given in the AB system.

The catalogue presenting the data obtained in this work is described in the Appendix and is available at the CDS.

2. Observational material and data reduction

The Subaru/*XMM-Newton* Deep Survey (SXDS; Sekiguchi, in prep.) is a large survey, covering a contiguous region of >1 square degree centred at RA = 02^h18^m and Dec = –05°00′, with a limiting AB magnitude at 3σ of 28.4 in the B band and a typical seeing of 0.8 (Furusawa et al. 2008). The SXDS field was observed at different wavelengths, from X-rays to radio. We briefly describe the data sets used in this work below. The X-ray and optical broad-band data (Furusawa et al. 2008; Pović et al. 2009b) are the main data used in our analysis to detect and select the AGN populations, and to derive their nuclear and morphological properties. Additionally, near- and mid-IR data have been used to measure k-corrections and photometric redshifts.

2.1. X-ray data

The SXDS was observed by *XMM-Newton* during the years 2000, 2002, and 2003 (PI Michael G. Watson). Seven pointings were obtained in the 0.2–10 keV energy range. The central observation is the deepest one, with a nominal exposure time of ~100 ks, and is surrounded by six shallower observations, each of them with an exposure time of ≈50 ks. The surveyed area is ≃1.14 deg^2, covering the complete region of five mosaic, optical images taken with the Subaru telescope (see below).

The required data were gathered from the *XMM-Newton* v.5.0 scientific archive (XSA[4]). Data processing was carried out by means of the Science Analysis System (SAS[5]) v7.1.2 package, using the latest relevant current calibration files (CCF). The raw observation data files (ODF) were processed using the standard SAS tasks *emproc* (for MOS cameras) and *epproc* (for *pn* camera) to produce calibrated event lists. Light curves were obtained by means of *xmmselect* and *OGIP light curve* tasks, selecting only events with pattern 0–4 (single and double) and PI 200-12000 for the pn camera, and pattern 0–12 and PI 200-15000 for the MOS cameras. Good Time Intervals (GTIs) were created using the *tabtingen* task, filtering event lists with RATE parameter. To merge event lists and additional files, we used the *merge* task. Six energy bands were selected, as shown in Table 1. Moreover, combining soft and hard bands we obtained fluxes in the 0.5–4.5 keV energy range. This band is the most widely used in our analysis for comparing our results with previous ones. Figure 1 shows the distribution of fluxes in five energy bands, for all detected X-ray sources, and for 262 sources analysed in this paper (see Sect. 2.7). The *evselect* task was used to produce the images and *fits* files in all selected energy ranges, separately for each instrument, and selecting only events with FLAG = 0. We computed the survey area as a function of the completeness flux in the total band (see Fig. 2) by evaluating the histogram of the survey distribution for increasing area values. The completeness flux for that area is derived as the energy bin corresponding to the maximum of the histogram. The survey is complete at $f_{0.5-10\,\mathrm{keV}} \approx 3.6 \times 10^{-15}\,\mathrm{erg\,cm^{-2}\,s^{-1}}$ for the maximum survey area, ~1.4 deg^2.

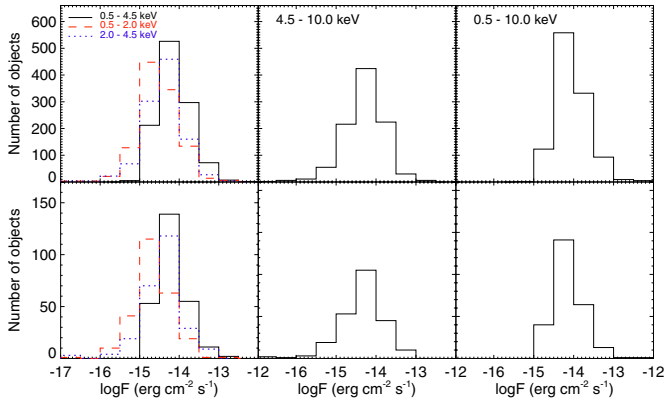

Fig. 1. X-ray flux distributions for all 1121 X-ray detected sources (*top*) and for 262 objects with $z \leq 2.0$ analysed in this paper (*bottom*; see Sect. 2.7). Flux distributions are represented in the 0.5–2.0 keV (dashed red line), 2.0–4.5 keV (dotted blue line), and 0.5–4.5 keV (solid black line) energy bands (*left panels*), 4.5–10.0 keV (*middle panels*), and 0.5–10.0 keV range (*right panels*).

Source detection was performed by means of the *edetect_chain* SAS procedure. To minimize the number of spurious detections, the likelihood threshold parameter[6] was set at $L = 14$. Thus, the probability that the source exists is at least $P = 0.9999916847$, or less than one fake source per instrument, per pointing, and per band. To convert count rates to energy fluxes, we computed energy conversion factors (ecf) using PIMMS (Mukai 1993), using power law function with a spectral index $\Gamma = 1.8$ (e.g., Mateos et al. 2005), and a Galactic absorption $nH = .5 \times 10^{20}\,\mathrm{cm^{-2}}$ (Dickey & Lockman 1990). PIMMS measured all *XMM-Newton* ecf values using the aperture of 15 arcsec, and ecf values had to be multiplied by a factor of 1.47 (aperture correction) to obtain a good superposition with the *XMM-Newton* PSF and integrate the flux of the source to large distances (Saxton, priv. comm., and *XMM-Newton* team for more information). The number of sources in each energy

[2] Optical System for Imaging and low Resolution Integrated Spectroscopy.
[3] Gran Telescopio de Canarias; http://www.gtc.iac.es/
[4] http://xmm.esac.esa.int/xsa/
[5] http://xmm.esac.esa.int/external/xmm_data_analaysis
[6] $L = -\ln(1-P)$, where P is the probability of having a spurious detection owing to random Poisson fluctuations.

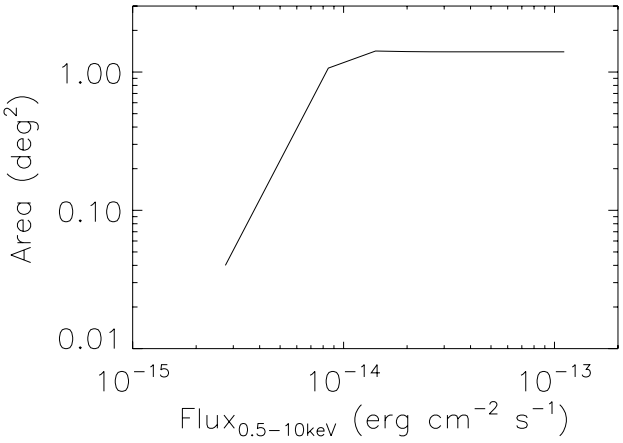

Fig. 2. Survey area as a function of flux in the total (0.5–10 keV) band.

band, final ecf values, and median and limiting fluxes are listed in Table 1 for each energy range. Hardness ratios[7] were also defined. We used HR(hard/soft) ≡ HR(2−4.5 keV/0.5−2 keV) throughout our analysis.

Source detection was performed separately in each field, and for each instrument. Double detections were eliminated from the overlapping regions, by removing detections with shorter exposure time from the source lists. Finally, source files obtained for each instrument were cross-matched, therefore creating only one file and keeping only detections with signal-to-noise ratios $S/N > 2$ in the total 0.5–10.0 keV range. The final catalogue has 1121 unique X-ray emitters, including sources detected in at least one of six energy bands.

2.1.1. Comparison with Ueda et al. results

Ueda et al. (2008) published a catalogue of X-ray emitters in the SXDS field. The complete catalogue consists of 1245 X-ray sources detected in one of six selected energy bands: 0.3–0.5 keV (ultrasoft), 0.5–2 keV (soft), 2–4.5 keV (medium), 4.5–10 keV (ultrahard), 0.5–4.5 keV (XID), or 2–10 keV (hard). The data in the first four bands are publicly available. In general, the data reduction carried out in Ueda et al. (2008) and prior to our analyses are quite similar. However, there are two main differences related to the source detection. First, Ueda et al. (2008) performed the source detection in the summed *pn* and MOS images, while we used individual images and finally summed detections from each camera, as explained above. Second, Ueda et al. (2008) adopted a detection likelihood threshold of 7 in a single band, while we used a more restrictive value, accepting only sources detected with a maximum likelihood above 14, and keeping only detections with $S/N > 2$ in the total 0.5–10.0 keV range.

Figure 3 shows $\log N - \log S$ relations in soft (0.5–2 keV) and total (0.5–10 keV) bands, where the total band for Ueda et al. (2008) data presents the sum of information obtained in their soft, medium, and ultrahard bands. Although in the soft band the Ueda et al. (2008) data are more sensitive, our X-ray emitters with optical counterparts are in good correlation with the whole Ueda et al. (2008) sample. However, a higher density of sources was detected in our full sample, probably owing to the differences between source detection procedures explained above. On the other hand, the limiting fluxes are in good correlation in the total band, and a higher density of sources was detected by Ueda et al. (2008) work, relative to both our full sample and optical counterparts, probably because of the less sensitive detection threshold used by the authors.

[7] Defined as $HR(\Delta_1 E/\Delta_2 E) = \frac{CR(\Delta_1 E)-CR(\Delta_2 E)}{CR(\Delta_1 E)+CR(\Delta_2 E)}$, where $\Delta_1 E$ y $\Delta_2 E$ are different energy bands and $CR(\Delta_n E)$ is the count rate in a given energy band.

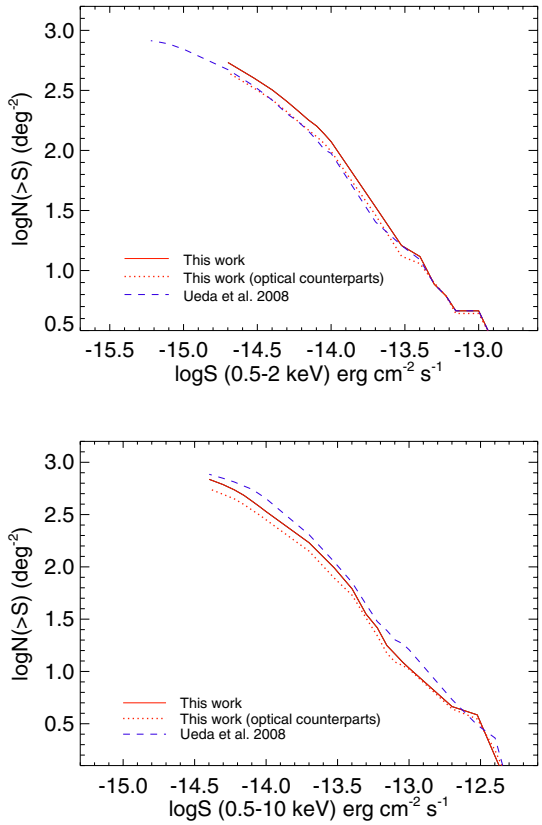

Fig. 3. Cumulative $\log N - \log S$ functions for X-ray sources detected in the SXDS field in the soft 0.5–2 keV (*top*) and total 0.5–10 keV (*bottom*) bands. Solid and dotted red lines show the data obtained in this work, presenting the full X-ray sample and the sample with optical counterparts, respectively. The dashed blue line presents the data obtained by Ueda et al. (2008) in the same bands.

Using a cross-matched radius of 5 arcsec, 857 counterparts (808 unique ones) have been found between Ueda et al. (2008) and our catalogues. The sources contained in the Ueda et al. (2008) catalogue that are missing in ours are in general fainter (e.g., around 90% of these objects have fluxes below our limiting flux in the soft band). On the other hand, sources contained in our catalogue but not contained in the Ueda et al. (2008) catalogue are in general of lower S/N (e.g., ∼50% and ∼75% of objects have S/N between 2–3 and 2–4, respectively). A good correlation was found for all counterparts between fluxes, with the linear correlation coefficients of 0.99, 0.97, 0.93, 0.96, and 0.99 in the 0.5–2 keV, 2–4.5 keV, 4.5–10 keV, 0.5–10 keV, and 0.5–4.5 keV bands, respectively, where the correlation coefficient of 1.0 represents a perfect linear correlation. In the soft band, the Ueda et al. (2008) data are more sensitive, as mentioned above, while in the ultrahard and total bands limiting fluxes are in a good agreement. We are unable to compare our and Ueda et al. (2008) X-ray luminosities, since they were not measured by the authors.

Table 1. Selected energy bands, number of detected sources in each band, computed energy conversion factors, and flux properties of X-ray emitters in the SXDS field.

Band	Energy range (keV)	Num. of sources	MOS ecf (10^{11} ct erg^{-1} cm^2)	*pn* ecf (10^{11} ct erg^{-1} cm^2)	Median flux (10^{-15} erg cm^{-2} s^{-1})	Limiting flux (10^{-15} erg cm^{-2} s^{-1})
soft	0.5–2.0	1103	2.102	5.977	2.84	2.25
hard	2.0–4.5	1048	0.786	1.41	4.37	4.0
veryhard	4.5–10.0	976	0.193	0.433	5.59	5.0
total	0.5–10.0	1121	1.076	2.781	7.8	5.0
veryhard2	4.0–7.0	957	0.358	0.668	16.2	10.0
total2	0.5–7.0	1121	1.266	3.258	10.6	9.0

2.2. Optical data

Optical imaging observations were carried out with the Suprime-Cam installed at the Subaru Telescope at Mauna Kea (Furusawa et al. 2008). Five continuous sub-fields were observed, covering an area of 1.22 deg^2 with a total integration time of 133 h. Each sub-field corresponds to a single Suprime-Cam field of view $\sim 34' \times 27'$, in five broad-band filters B, V, R_c, i', and z', with limiting AB magnitudes at 3σ of: 28.4, 27.8, 27.7, 27.7, and 26.6, respectively. Publicly available catalogues were downloaded from the SXDS web page[8], each of them containing five-band aperture photometry (performed through fixed 2 and 3 arcsec apertures). The total number of objects are 940 853, 1 002 561, 901 094, 899 484, and 842 590, in the B, V, R_c, i', and z' bands, respectively.

2.3. Near-IR data

We used near-IR (NIR) data from the XMM-LSS survey (which encompasses the SXDS field), being part of the United Kingdom IR Telescope Deep Sky Survey (UKIDSS). Specifically, we downloaded and used the UKIDSS *JHK* Second Data Release (DR2) catalogue[9]. The photometric system is described in Hewett et al. (2006), and the calibration is described in Hodgkin et al. (2009). The AB limiting magnitudes at 2σ are 23.4, 23.4, and 22.9 in J, H, and K bands, respectively.

2.4. Mid-IR data

The SXDS field was observed with the *Spitzer* telescope as part of the XMM-LSS field, one of the areas surveyed within the *Spitzer* Wide-area IR Extragalactic Legacy Survey (SWIRE). The public IRAC catalogue was downloaded from the SWIRE web page[10] and used in this work. It provides a set of fluxes within four different aperture radii, 1.4, 1.9, 2.9, and 5.8 arcsec for the four IRAC channels (3.6, 4.5, 5.8, and 8.0 μm). Any source included in the catalogue was detected in both the 3.6 μm and 4.5 μm bands. To convert the given fluxes to magnitudes, we used the equation

$$m[i] = 2.5 \log_{10}(F^{[i]}_{\rm zero}/F^{\rm quot}_{\nu}), \quad (1)$$

where $i = 3.6$, 4.5, 5.8, and 8.0 are the four IRAC channels (Reach et al. 2005). $F^{\rm quot}_{\nu}$ is the flux density of a source from the calibrated images, and $F^{[i]}_{\rm zero}$ are the zero-magnitude flux densities. The zero-magnitude fluxes were determined by Reach et al. (2005) by integrating the Kurucz model spectrum of αLyr over the IRAC pass-bands. The resulting zero-magnitude flux densities used in this work are 280.9 ± 4.1, 179.7 ± 2.6, 115.0 ± 1.7, and 64.13 ± 0.94 Jy in the 3.6, 4.5, 5.8, and 8.0 μm channels, respectively. The total SWIRE XMM-LSS catalogue has ~250 700 objects. The AB limiting magnitudes at 2σ are 21.0, 21.1, 19.5, and 19.4 in the 3.6, 4.5, 5.8, and 8.0 μm bands, respectively.

2.5. The catalogue of optical counterparts

Owing to the very high number of detections in the optical bands (around 900 000 sources in both the R_c and i' bands, as noted in Sect. 2), there is a high probability of an erroneous identification when matching the X-ray and optical catalogues. To minimise such a risk, the optical catalogue was first filtered. On the basis of previous results in the GWS field (Pović et al. 2009a), the optical flux was constrained by assuming an upper limit to the X-ray-to-optical flux ratio[11], $X/O = 18$. We found that this X/O ratio is a reasonable limit, since no sources were found above this value in the GWS field. With this cut and the minimum X-ray flux of 8.9×10^{-16} erg cm^{-2} s^{-1} detected in the SXDS field, we obtained an upper limit in the optical range, and excluded all optical detections having AB magnitude $R_c > 27.17$. After applying this filter, the resulting catalogue had been reduced in size from 901 094 R band sources to 614 857. This approach was found to be consistent with that adopted for the SXDS sample, since none of the X-ray sources with $F_{0.5-4.5\,\rm keV} \leq 6.0 \times 10^{-15}$ erg cm^{-2} s^{-1} show $X/O > 18$, while only about 5% of the total number of sources exceed this limiting X/O value.

After filtering the optical catalogue, we followed a cross-matching procedure similar to that described in Pović et al. (2009a). After comparing the number of unique counterparts with the number of multiple matches, radii of between 2″ and 3″ were found to be the best compromise, enabling us to select as always a source closest to the X-ray detection as an optical counterpart. After applying the statistical methodology from de Ruiter et al. (1977), a radius of 3″ was selected, obtaining a completeness of 99.9% and a reliability of 76.2%. The total number of optical counterparts obtained with this radius is 806. In addition, for objects with multiple matches inside the selected radius, we performed the Sutherland & Saunders (1992) methodology measuring the reliability for all possible matches, and finally selecting as an optical counterpart an object with the highest probability. After this, the number of possible fake identifications drops to ~6%, where multiple matches are detected

[8] http://www.naoj.org/Science/SubaruProject/SXDS/index.html

[9] http://www.ukidss.org/archive/archive.html; Warren et al. (2007).

[10] http://swire.ipac.caltech.edu/swire/astronomers/data_access.html

[11] Computed as $F_{0.5-4.5\,\rm keV}/F_R$, where the optical flux F_R has been derived from the SExtractor auto magnitudes in the R band; see Sect. 4 for more information and references.

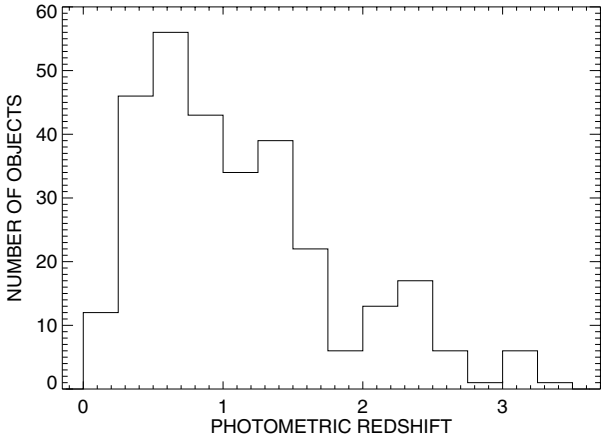

Fig. 4. Distribution of final photometric redshifts of X-ray emitters with optical counterparts.

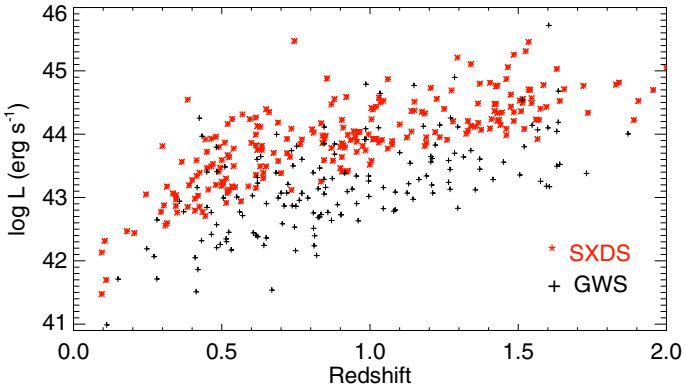

Fig. 5. Relation between the X-ray luminosity in the 0.5–7.0 keV band and redshift for a sample of AGN in the SXDS (red stars) and GWS (black crosses) fields.

with similar probabilities. Regarding the ~300 X-ray sources not optically matched, 80 objects reside in the area not covered by optical observations; the remaining objects might have been lost through optical catalogue filtering, be optically obscured sources, or in some cases have resulted from fake X-ray detections (see Sect. 2.1).

2.6. Photometric redshifts and k-corrections

We used the Bayesian code ZEBRA (Feldmann et al. 2006) to compute the photometric redshifts of the optical counterparts. Owing to the small number of available spectroscopic redshifts used in the analysis (for only 15 sources obtained from Aretxaga et al. 2007, and references therein), as an additional check, photometric redshifts were also computed using the HyperZ code (Bolzonella et al. 2000). In both codes, the templates from the SWIRE[12] template library were implemented and used, since they include the templates of AGN/QSO sources (Polletta et al. 2007). After comparing the results of ZEBRA and HyperZ, we accepted only those objects for which the redshift results from both codes agree to within less than 0.1 for $z < 1$ and 0.2 for $z \geq 1$. Finally, we derived high-quality photometric redshift information for the 306 objects shown in Fig. 4. The mean value of the final photometric redshifts is 1.17 ± 0.15. Among these, 86% of objects have photometric redshift errors of below 20%.

To obtain k-corrections for the optical fluxes, we used the IDL routine KCORRECT (Blanton et al. 2007). The X-ray fluxes, on the other hand, were k-corrected by assuming a standard power-law SED with $\Gamma = 1.8$. A rough classification between X-ray unobscured and obscured AGN was made using the hardness ratio HR(2−4.5 keV/0.5−2 keV) (see Sect. 4.3), which is quite sensitive to absorption (Della Ceca et al. 2004; Caccianiga et al. 2004; Dwelly et al. 2005); those objects with HR(2−4.5 keV/0.5−2 keV) ≤ 0.35 (some 53%) data were considered as unobscured, and no intrinsic absorption was applied to the power-law SED; otherwise the objects were considered as obscured and a fixed intrinsic absorption $N_{\rm H} = 1.0 \times 10^{22}$ cm^{-2} was included (e.g., Silverman et al. 2005; Younes et al. 2011).

2.7. Selected sample

After performing the methodologies of de Ruiter et al. (1977) and Sutherland & Saunders (1992) when cross-matching the X-ray and optical catalogues, and after considering only those objects with high-quality photometric redshift information, we had 306 remaining sources in our sample. Of these, 262 sources (85%) have photometric redshifts ≤2.0. We obtained the morphological classification for all 306 objects (see Sect. 3), but carried out all further analysis for a sample of objects with redshifts $z \leq 2.0$ and redshift errors below 20%. For this sample, we derived X-ray luminosities in all selected energy ranges. The average luminosity of $\log L_{\rm X} = 43.7$ erg s^{-1} was measured in the 0.5–7.0 keV band. Figure 5 shows the luminosity-redshift plane of the X-ray detected AGN in the SXDS and GWS fields at $z \leq 2.0$.

The selected $z \leq 2.0$ sample represents around 25% of the initial X-ray sample, and 32% of the optically matched sample. To determine whether this sample is representative of the full X-ray population or the matched one, we compared their X-ray flux distributions in all energy bands. Figure 1 shows these distributions in five energy bands for the parent X-ray sample and the analysed one. The selected sample seems to follow the distribution of the full X-ray population in all observed bands quite well. When performing Kolmogorov-Smirnov statistics, we obtained the probability parameter of 0.7 and 0.97[13] in the 0.5–4.5 keV band (the energy range used in the AGN selection; see Sect. 4) when comparing the analysed sample with both the full X-ray population and the full optically matched sample, respectively. Moreover, we compared the X-ray and optical properties of the selected and full optically matched samples. Figure 6 (top) shows the relation between the X-ray flux in the 0.5–4.5 keV energy range and the AB $R_{\rm c}$ magnitude for these two samples. As can again be seen, the selected $z \leq 2.0$ sample covers the entire range of X-ray fluxes, in contrast to the matched one. For a selected sample, there seems to be a shallow bias towards fainter sources in the optical range. However, when comparing the X-ray-to-optical flux ratios (Fig. 6, down panel), the selected sample represents the full matched one quite well. For these two samples, the average $\log X/O$ ratios are 0.05 and −0.07, respectively.

To summarise, the $z \leq 2.0$ selected sample is a small fraction (~25%) of the full X-ray population (as mentioned above), but

[12] http://www.iasf-milano.inaf.it/~polletta/templates/swire_templates.html

[13] Probability can be between 0.0 and 1.0, where 1.0 means that the compared distributions are completely identical.

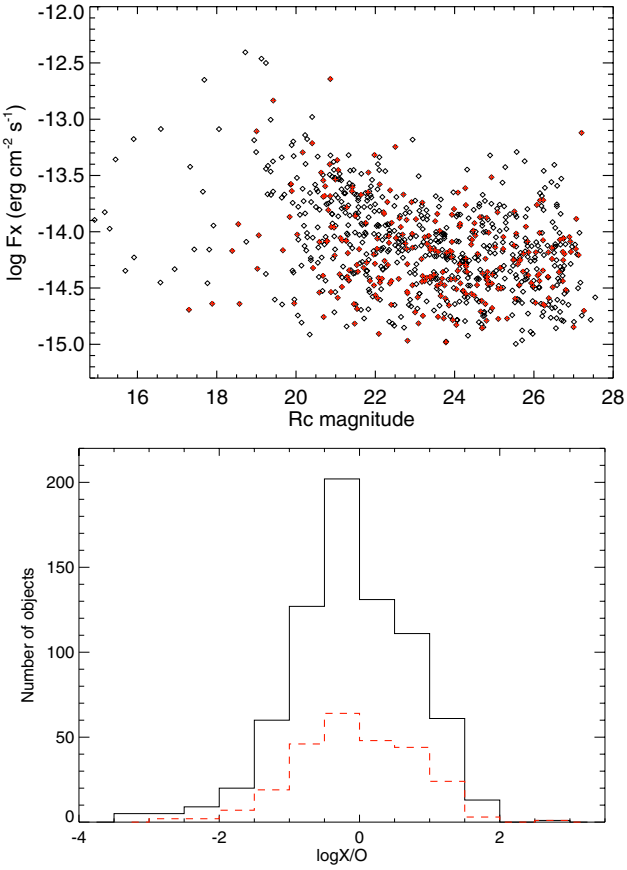

Fig. 6. *Top*: relation between the X-ray flux in the 0.5–4.5 keV energy range and the AB R_c magnitude of the full matched sample (black diamonds) and the selected sample (red crosses). *Bottom*: distributions of the X-ray-to-optical flux ratios of both the full matched sample (black solid line) and the selected sample (dashed red line).

seems to follow the distributions of the initial X-ray and optically matched samples quite well.

Finally, to improve statistics, we included our data from the Groth-Westphal Strip (GWS) field when analysing the colour–magnitude relations. We considered 174 objects with photometric redshifts ≤2.0 and redshift errors below 20%. These data are deeper in X-rays than the SXDS data, and have an X-ray limiting flux of 0.48×10^{-15} erg cm^{-2} s^{-1} in the 0.5–7.0 keV energy band. The detailed description of the data and both the morphological and nuclear classifications can be found in Pović et al. (2009a). A small comparison between the luminosities in the SXDS and GWS fields is also presented below (see Fig. 5 and Sect. 2.7).

3. Morphological classification and analysis

3.1. Methodology

The morphology of the optical counterparts of X-ray emitters in the SXDS field was tested using both the SExtractor (Bertin & Arnouts 1996) and galSVM (Huertas-Company et al. 2008, 2009) codes. Moreover, as an additional check, a visual classification was also performed.

Compact objects were first separated from extended ones. The SExtractor CLASS_STAR parameter was used to this end. This parameter permits the rough classification of objects as either compact (QSOs, AGN with the weak host galaxies, stars, etc.) or extended. The computed value depends on the seeing, the peak intensity of the source and its isophotal area. The parameter ranges between 0 (for an extended object like a galaxy) and 1 (for a point-like object). A source was deemed as compact if its CLASS_STAR parameter is ≥0.9.

To distinguish between early- and late-type X-ray emitters (see Sect. 3.2 below), we used the galSVM code (Huertas-Company et al. 2008, 2009). galSVM[14] is a freely available code written as an IDL library that, combined with the similarily freely available library libSVM[15] enables a morphological classification of galaxies in an automated way using support vector machines (SVM[16]). This code represents a great improvement to non-parametric methods for morphological classification, being especially useful when dealing with low-resolution, and high-redshift data. It makes it possible to use a sample of objects with known morphologies, to match the properties of these objects to the redshift and image quality of the sources that have to be classified, to test simultaneously different morphological parameters and find the best set for the morphological classification, and to use non-linear boundaries to distinguish between different types. Different morphological parameters have been suggested and used in morphological classification in recent years (Abraham et al. 1996; Kent 1985; Bershady et al. 2000; Graham et al. 2001b; Abraham et al. 2003; Conselice et al. 2003; Lotz et al. 2004), each of which provide different types of information about the structure of a galaxy. Before the development of galSVM, it had been impossible to use more than three parameters simultaneously, forcing the boundaries between different Hubble types to be linear (two-dimensional regions or hyperplanes). Therefore, besides being useful when dealing with high-redshift and low-resolution data, there are two main advantages of galSVM compared to other codes: first, it can use a list of morphological parameters simultaneously, and second, it can find and use non-linear boundaries to perform the final morphological classification. It has been shown that using galSVM to classify galaxies into two main morphological types (early- and late-type galaxies), provides a more reliable classification than other non-parametric methods (Huertas-Company et al. 2008). Therefore, since we analysed low-resolution and high-redshift data, we decided to use the galSVM code to separate early- from late-type X-ray emitters in the SXDS field. galSVM requires the availability of redshift information for all examined objects, thus we attempted to determine the morphology of the 306 X-ray sources with known photometric or spectroscopic redshifts. To perform the analysis, data for the i' optical band were chosen owing to its larger S/N.

We followed the complete and standard galSVM procedure, as described in Huertas-Company et al. (2008), to differentiate between early- and late-type X-ray emitters with optical counterparts:

1. We compiled a set of simulated galaxies, using a catalogue of local galaxies with known Hubble types (obtained by visual classification), redshift, total flux, and half luminosity radius. The Tasca & White (2011) catalogue was used for this purpose, containing 1504 visually classified local galaxies from

[14] http://gepicom04.obspm.fr/galSVM/Home.html

[15] Support Vector Machines library (libSVM), written by Chih-Chung Chang & Chih-Jen Lin, is an integrated program for support vector classifications, regressions, and distribution estimations; it supports the multi-parameter classifications.

[16] Support Vector Machines (SVM) are a group of supervised learning methods that can be applied to classification or regression. Support Vector Machines represent an extension to non-linear models of the generalised portrait algorithm developed by Vladimir Vapnik (1995).

Table 2. Set of parameters used by galSVM for the final morphological classification of X-ray emitters in the SXDS field.

ELONGATION[1]	CLASS_STAR
ABRAHAM CONCENTRATION INDEX[2] ($\alpha = 0.3$)	ASYMMETRY[2]
SMOOTHNESS[3]	GINI COEFFICIENT[4]
M_{20} MOMENT OF LIGHT[5]	BERSHADY-CONSELICE CONCENTRATION INDEX[6]

Notes. [1] Ratio of the major to minor axes (A_IMAGE and B_IMAGE SExtractor parameters; Bertin & Arnouts 1996). [2] Abraham et al. (1996). [3] Conselice et al. (2003). [4] Abraham et al. (2003). [5] Lotz et al. (2004). [6] Bershady et al. (2000).

the SDSS survey, observed in the g photometric band, which corresponds to the rest-frame[17] band of the SXDS i' sample for the average redshift of 0.8. In addition to the local catalogue, subimages of all local galaxies and PSFs, which are the data necessary to run galSVM, was also gathered from Tasca & White (2011). For each of the five SXDS fields observed in the optical i' band, we provided the magnitude and redshift distributions of our X-ray emitters with optical counterparts. Moreover, we ran SExtractor for our real images in order to obtain the catalogue of all possible detections, as well as mask images. For every galaxy stamp used to train the morphology, galSVM generates a random pair of magnitude and redshift values with a probability distribution that matches that of our real data, to place the training galaxy in a real, high-redshift background image of our sources. Using the real images and SExtractor catalogues, the locations devoid of objects where the trained sample of galaxies could be placed are searched randomly, and a SExtractor mask image is then used to eliminate nearby objects.

2. After placing the sample of local galaxies in the high-redshift background of our real sample, we measured a set of morphological parameters of the training sample.
3. We trained a SVM with a fraction of 600 local galaxies and used the other fraction of 904 local galaxies to test the accuracy[18] and estimate the errors. We then repeated steps two and three to test different sets of morphological parameters and choose the one that gives the most reliable morphological classification, which we used afterwards to classify our real sample. As already mentioned, the galSVM accuracy parameter was used as an indicator of the classification reliability, but in addition to the accuracy, the distributions of the derived morphological parameters were tested. It was seen that there is a trend for bright objects to be identified as late-types with very high probabilities, increasing the value of the mean probability. Therefore, all brightness parameters (such as mean surface brightness, magnitude, and flux) were excluded from the initial set of parameters involved in the morphological classification. Table 2 shows the final set of parameters used to separate between early- and late-type galaxies. For this set of parameters, an accuracy of 70% was achieved (see Sect. 3.2 below).
4. A set of morphological parameters was obtained for all X-ray emitters with optical counterparts. In addition, using the parameters given in Table 2, we performed a morphological classification using galSVM, correcting where possible for systematic errors detected in the testing steps.

3.2. Morphology of X-ray emitters

In our morphological classification early-type galaxies consist of ellipticals and lenticulars (although in some cases early-type spirals between S0 and Sa galaxies might also be classified as early-type), while spiral and irregular galaxies were classified as late-type. The classification procedure assigns to each galaxy a class label and a probability of belonging to a given class. When dealing with a two-class problem (early- and late-type classification; see Huertas-Company et al. 2008), the probability p is $p_{\rm early-type} = 1 - p_{\rm late-type}$. Therefore, two probabilities are measured namely $p_1 = p_{\rm early-type}$ and $p_2 = p_{\rm late-type}$ where for a galaxy to be considered as early- and late-type the probability p_1 and p_2 must be higher than 0.5, respectively. The probability parameter is used to assess the accuracy of the morphological classification. There is a clear correlation between the probability threshold and the number of correct identifications: the accuracy clearly increases when the considered probability is higher. Huertas-Company et al. (2009) demonstrated that selecting objects with a probability of between 0.5 and 0.6 yields a mean accuracy of around 58%, while objects with probabilities greater than 0.8 are classified with nearly 90% accuracy.

As already mentioned in Sect. 3.1, the SExtractor STAR_CLASS parameter was used to separate compact from extended (host-dominated) objects. We found that 22% of the total number of objects were compact, having a STAR_CLASS parameter $\geq$0.9. Among these objects detected as early-type (with STAR_CLASS < 0.9 and $p_1 > 0.5$; 53% in total), 56% have probabilities $\geq$0.75. In contrast, among the objects identified as late-type (with STAR_CLASS < 0.9 and $p_2 > 0.5$; 18% in total) only 30% were found with probabilities $p_2 \geq 0.75$. The population of unclassified objects is 7% in total.

Several trends in the mean probability values were tested (for both early- and late-types) with redshift, magnitude, and isophotal area (see Fig. 7, upper panels). Since the trends in the morphological parameters with distance, brightness, and size were also present in the training sample, the algorithm should be aware of these trends and be able to take them into account in the final classification. For p_1 probabilities (early-type objects), there is only a weak trend with these parameters. Yet for p_2 probabilities (late-type objects), the trends seem to be more significant. This means that low p_2 probability objects (e.g., $p_2 < 0.7$) still have a high probability of being one of the late-types, but are detected with low probabilities since they are more distant, smaller, and/or fainter sources.

To check the obtained probabilities, a visual inspection of the images was performed. This has been the traditional way of classifying galaxies into different morphological types and it is rather subjective, but for bright and extended objects it

[17] As noted by Huertas-Company et al. (2008), selecting the training sample as the rest-frame band data has three main advantages: *(i)* it is less affected by k-correction effects, *(ii)* it does not introduce any modelling effects, since the analysed galaxies are real, and *(iii)* it is possible to work with seeing-limited data (as the training set is built to reproduce the observing conditions and physical properties of the sample to be analysed, but is classified using well-resolved images).

[18] The accuracy represents the success rate in the morphological classification of the training sample; see Huertas-Company et al. (2008) for more information.

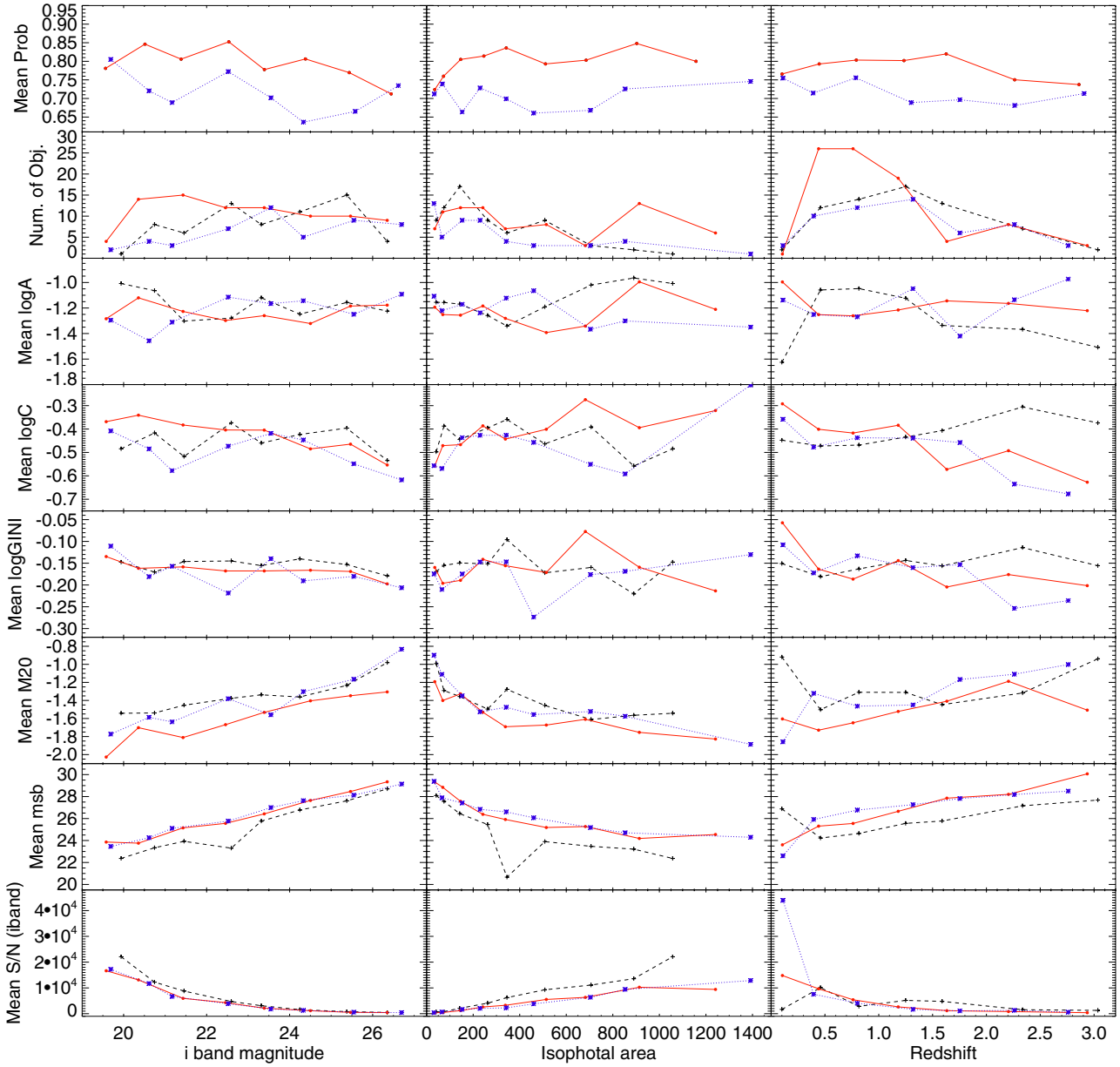

Fig. 7. *From top to bottom*: relationship between mean values of galSVM probabilities, number of objects, asymmetry index, Abraham concentration index, Gini coefficient, M_{20} moment of light, mean surface brightness, and S/N in i band. *From left to right*: apparent magnitude in i' band, isophotal area, and redshift. Compact objects are marked with black crosses and dotted lines, early-type galaxies with red spots and solid lines, and finally, late-type galaxies with blue stars and dashed lines.

can produce a high confidence-level morphology, and may be a helpful tool for probing the reliability of different structural parameters computed with automated methods. To this end, the IRAF/*imexam* tool was used to create the isophotal contour diagrams, providing information about bulge/disc-dominated objects (for more information, see Pović et al. 2009a). For objects classified as both compact and late-type, there is a good correspondence between the automated and visual classifications. Conversely, for objects classified with galSVM as early-type galaxies having p_1 probabilities ≥0.75, there is a good correlation with visual inspection, while in cases of lower p_1 probabilities ($0.5 < p_1 < 0.75$), the number of possible interactions starts to grow, as well as the number of objects with low S/N, which are possible late-type objects. Therefore, in our more detailed analysis only high-probability ($p_1 \geq 0.75$), early-type objects were considered in the early-type class.

Figure 8a shows a standard morphological classification diagram, comparing the asymmetry parameter (A) and Abraham concentration index (C). This figure was used to roughly distinguish the areas where most of the early- (only objects with $p_1 \geq 0.75$; red dots) and late-type galaxies (all objects with $p_2 > 0.5$; blue stars) are located. The separation differs from that defined by Abraham et al. (1996; see their Fig. 5). This is expected for at least two reasons: first, a number of early-type spirals (between S0 and Sa galaxies) enter into the early-type classification obtained by galSVM , and/or second, different methods have been used to obtain concentration and asymmetry indices. As already mentioned, the morphological classification in this work was also not solely based on this two-parameter diagram, but rather on eight parameters that were used by galSVM (see Table 2). As discussed in more detail in Sect. 3.3, it seems that a multi -parameter space with non-linear separations is necessary

to separate early- from late-type galaxies accurately. This is one of the main galSVM advantages in comparison to other morphological classification codes. In the same figure we also show objects with early-type class probabilities of $0.5 < p_1 < 0.75$ (open diamonds). These objects cover both areas, with a possibility of being either early-, late-type galaxies, or interacting systems, as explained above.

3.3. Difficulties in the morphological classification

3.3.1. Systematic trend with brightness, size, and redshift

The relations between the different morphological parameters and apparent magnitude (in the i' band), size (isophotal area), and distance (redshift) have been tested for a sample of SXDS X-ray emitters analysed in this paper, belonging to the different morphological types of compact, early- ($p_1 \geq 0.75$), and late-type objects ($p_2 > 0.5$). Figure 7 shows the aforementioned relations for the asymmetry and Abraham concentration indices, Gini coefficient, M_{20} moment of light, and mean surface brightness. The mean number of objects and S/N ratio in i' band are also represented. There is a certain trend of observed morphological parameters with the apparent magnitude, size, and distance. The parameters related to the galaxy concentration (C, Gini, and M_{20}) seem to be more affected than the asymmetry index. In other words, fainter, smaller, and more distant objects have systematically lower light concentrations. This might be due to detection effects, but might also be related to the intrinsic properties of the galaxies, since fainter and/or smaller objects are intrinsically less concentrated (e.g., Blanton et al. 2001). In general, the parameters of the objects that are detected as compact seem to depend more weakly on the brightness, size, and redshift than early- or late-types. On the other hand, early- and late-type galaxies seem to follow similar trends, although we again note that the code takes these trends into account in the final classification because identical ones are also present in the local training sample.

3.3.2. Low S/N

The bottom panels in Fig. 7 show how the S/N for the i' band change with brightness, size, and distance. As already mentioned in the previous two sections, a low S/N increases the uncertainty in the morphological classification. Two effects can therefore be observed:

- As the S/N decreases, the information about the galactic disc can be lost. This results in the possibility that a group of late-type galaxies may be classified as early-type, while early-type galaxies may also be classified as compact objects. Low S/N affects all morphological parameters, those related to the asymmetry/smoothness, as well as those related to the galaxy light concentration.
- Low S/N ratios can also affect the preciseness of the measured bulge properties. For example, it can be observed how the Abraham concentration index changes as the S/N decreases in a bulge-dominated or compact object. A low S/N might be expected to smooth out the galaxy profile affecting regions far away from the centre more severely. Thus, the galactic radius (used to calculate the concentration index as the ratio of the total flux to the flux at 30% of the radius) will also decrease. Both the $F_{\rm tot}$ and F_{30} fluxes will be affected, but F_{30} might decrease significantly, leading to smaller values of the galaxy light concentration. Therefore, bulge-dominated objects with low S/N ratios will have lower concentrations (than the ones with high S/N), placing them in the regions populated by late-type objects. Nevertheless, most of these diagrams can be used to define the region where most of the compact objects are located, as shown in Fig. 8.

Table 3. Summary table: Morphology of X-ray emitters with optical counterparts in the SXDS field.

Morphology	Comment
22% compact	
30% early-type	$p_1 \geq 0.75$
23% early-/late-type or possible interactions	$0.5 < p_1 < 0.75$
18% late-type	$p_2 > 0.5$
7% unidentified	

3.3.3. Number of parameters needed for the morphological classification

As already stated, various structural parameters were obtained with galSVM in order to characterise the morphology of the X-ray emitters in the SXDS field. The relationship between them was studied after obtaining the final morphological classification. It was seen that for the observed sample of objects the combination of any two parameters was insufficient to distinguish between early- and late-type galaxies. A classification in a multi-parameter space with non-linear separations was needed, as done with galSVM. However, besides the log A versus log C diagram (see Abraham et al. 1996), presented in Fig. 8a, the smoothness and M_{20} moment of the light parameters related to the Abraham concentration index, and the mean surface brightness related to the M_{20} moment of light make it possible to define the high probability regions in the plane of finding compact, early-, and late-type objects, as shown in Figs. 8b–d, respectively, although the dispersion among the classes is still significant. A linear correlation was also seen between the four parameters related to the galaxy concentration (Abraham and Bershady-Conselice concentration indices, Gini coefficient, and M_{20} moment of light), as well as between the mean surface brightness and both C and Gini (see Figs. 8e,f). However, apart from the M_{20}-C diagram, for the observed sample they do not provide a good method for separating early- from late-type morphologies.

3.4. Morphological classification: summary

We describe our catalogue providing the final morphological classification and the list of morphological parameters and other data obtained in this work in Appendix A, which is available in the electronic edition of this paper.

After performing a morphological study of the X-ray emitters with optical counterparts in the SXDS field, it can be concluded that the sources analysed in this paper are predominantly hosted by luminous spheroids and/or bulge-dominated galaxies. At least 55% of the hosts are either compact or E/S0/S0-Sa galaxies. Table 3 summarises the final morphological classification of the selected sample, which is a subsample of the full X-ray population. Although the selected sample seems to be representative of the full X-ray population (see Sect. 2.7), the results presented here should not exclude the possibility that the remaining 73% of hosts for which morphological classification was impossible may be consist of later types.

As noted in Sect. 4.3, most (if not all) of the X-ray emitters analysed in this paper are AGN. Therefore, the results obtained

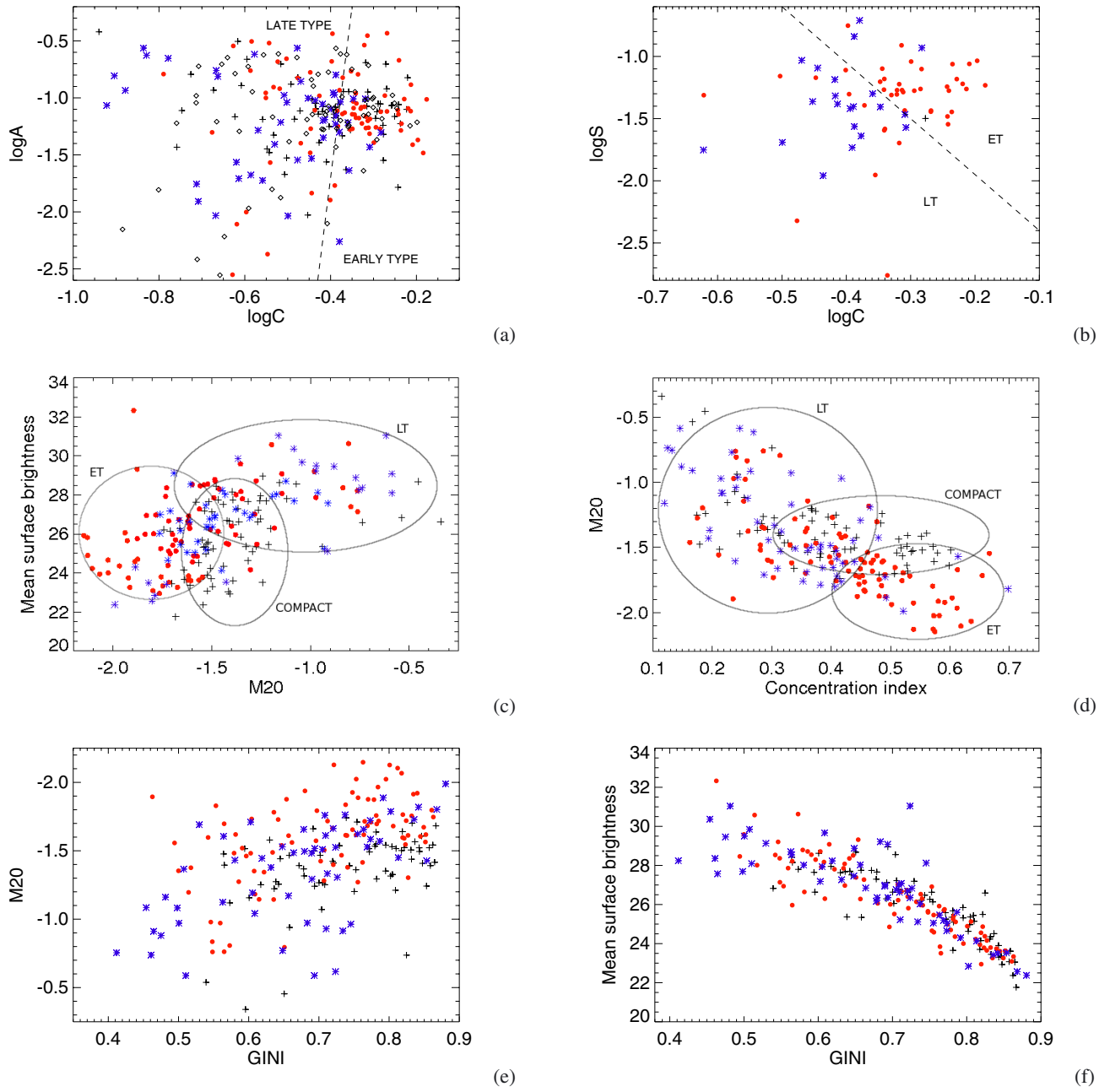

Fig. 8. *Top left*: relation between asymmetry and Abraham concentration index. Red dots represent the early-type galaxies (E/S0, S0/Sa) classified with probabilities $p_1 \geq 0.75$, while the blue stars represent all late-type galaxies having p_2 probabilities above 0.5. Black crosses represent compact objects (all sources with CLASS_STAR ≥ 0.9). Open diamonds are sources with $0.5 < p_1 < 0.75$, which might be either ET/LT or mergers (see Sect. 3.2). The dashed line separates the areas where most of the early- and late-type galaxies are located (right and left area from the dashed line, respectively). *Top right*: relation between the smoothness and Abraham concentration index. The dashed line separates the areas where most of the early- (on the right; red dots) and late-type (on the left; blue stars) galaxies are located. Relation between the mean surface brightness and M_{20} moment of light (*middle left*), and between the M_{20} moment of light and Abraham concentration index (*middle right*). Symbols are the same as on the previous two plots. High probability regions of finding any of three morphological groups (early-, late-, or compact sources) have been defined in both plots. *Bottom left*: relation between the M_{20} moment of light and Gini coefficient. See previous plots for symbols description. *Bottom right*: relation between the mean surface brightness and Gini coefficient. See previous plots for symbols description.

in this work can be compared with previous results on the host galaxy morphologies of X-ray selected AGN.

In general, the morphological classification performed in this work confirms some of the latest findings that indicate that most X-ray detected AGN are hosted by spheroids and/or bulge-dominated galaxies (e.g., Grogin et al. 2005; Pierce et al. 2007; Gabor et al. 2009; Pović et al. 2009a; Georgakakis et al. 2009; Griffith & Stern 2010). Pierce et al. (2007) used a sample of 94 intermediate-redshift AGN ($0.2 \leq z < 1.2$), selected using *Chandra* X-ray data and Spizer MIR data in the Extended Groth Strip (EGS) field. Basing their classification on the M_{20} moment of light and Gini coefficient, they found that X-ray selected AGN mostly reside in bulge-dominated galaxies ($53^{+11\%}_{-10\%}$), which is in good agreement with our study taking into account galaxies classified as both compact and early-type. Our results are also in good agreement with Georgakakis et al. (2009), who used the

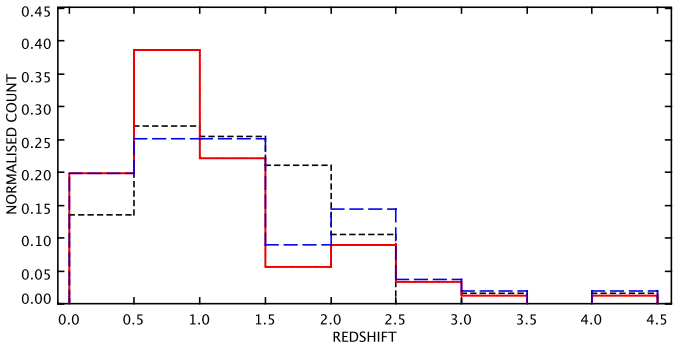

Fig. 9. Normalised redshift distributions of compact (short-dashed black line), early- (solid red line), and late-type (long-dashed blue line) sources.

high-resolution optical data from the Hubble Space Telescope (HST) to study the morphological properties of a large sample of X-ray detected AGN. They found that a majority of their objects are bulge-dominated galaxies. Compared with the latest analysis performed by Griffith & Stern (2010), we found a smaller number of compact sources, but larger number of early-type bulge-dominated galaxies.

Most of the objects morphologically classified have redshifts $z < 2.0$ (although a small fraction of 16% have photometric redshifts $z < 2.0$), which indicates that nuclear activity remains preferentially associated with bulge-dominated galaxies out to substantially high look-back times. Figure 9 shows the normalised distribution of different morphological types with redshift, suggesting that the objects from our sample classified as early-types reach a peak around $z \sim 0.8$, while the maximum distribution of late-type objects peaks at higher redshifts of $z \sim 1.2$. Most of the objects detected as compact were found around $z \sim 1.0$.

As shown in Georgakakis et al. (2009) and references therein, studying the morphology of the AGN host galaxies can be an important way of addressing the issue of the AGN fuelling mechanisms, by placing robust limits on the relative contributions of the different mechanisms (e.g., major mergers, minor interactions, internal instabilities) to the accretion history. In the standard view of hierarchical structure formation, spheroidal and early-type bulge-dominated galaxies suffered major mergers in their past that destroyed any pre-existing discs to form a bulge-dominated remnant (e.g., Barnes & Hernquist 1996; Springel & Hernquist 2005; Hopkins & Hernquist 2009). Hence, we can conclude that different mechanisms may be responsible for putting a galaxy in an active phase. As shown above, at least 50% of the X-ray detected AGN analysed in this work reside in spheroids and/or bulge-dominated systems, suggesting that they might have undergone major mergers in their accretion history. However, at least 18% of the AGN seem to have disc galaxy hosts, showing therefore that minor interactions, internal instabilities, and/or some other secular mechanisms could also play an important role in accretion and black hole feeding.

4. AGN colour–magnitude relations (CMRs)

As we have already mentioned, besides morphology, colours are essential for studying the properties of AGN host galaxies and their connection to the AGN phenomena. Using a large sample of X-ray selected AGN, we analysed colour–magnitude diagrams in order to study their relationship to the other properties of active galaxies. The sample used in this study has two main advantages, compared to those used in previous works it is much larger and it represents one of the deepest optical datasets to date.

To measure the colours of AGN, only objects with $\log X/O \geq -1$ were examined, the typical values of active galaxies, where X-ray fluxes are measured in the 0.5–4.5 keV energy range and the optical fluxes in the R band (e.g., Fiore et al. 2003; Della Ceca et al. 2004). In addition to the AGN sample selected in the SXDS field, we used a sample of AGN selected in the GWS field (Pović et al. 2009a). This extended sample was compared with a population of normal galaxies belonging to the CDF-S field (Wolf et al. 2001, 2004, 2008). The SXDS optical data are deeper than CDF-S data (and deeper than most (if not all) other ground based photometry optical surveys), although only 20% of active galaxies in our sample have magnitudes brighter than the completeness limit of the CDF-S data. Nonetheless, the information necessary to make these comparisons is publicly available for a large number of normal galaxies in the CDF-S field. The CDF-S catalogue contains 50 000 objects, among which those classified by the COMBO-17[19] survey as "galaxy" (44 925 sources) were included in our comparison sample. Following Wolf et al. (2001, 2004, 2008), the selected sample could contain up to a few dozen Seyfert-1 objects, as Seyfert-2 galaxies. However, compared with the population of normal galaxies, we expect these objects to make only a small contribution (Wolf et al. 2001, 2004, 2008). Therefore, we do not expect such a small fraction of these active galaxies to contaminate significantly the sample of non-active galaxies selected and used in this work, thereby changing the derived conclusions. Moreover, since the sample of normal galaxies was classified by the COMBO-17 survey using all the available spectrophotometric information in 17 filters, it should be suitable for comparing the colours of normal and active galaxies, without introducing any selection bias.

We note again as in Sect. 2.7 that in all colour–magnitude diagrams, we analysed only objects with photometric redshifts $z \leq 2$ and errors smaller than 20%, to help remove possibly less reliable measurements. There are 262 objects in total fulfilling these conditions.

4.1. CMRs in relationship with redshift

Figure 10 shows the CMR of the rest-frame $B - V$ colour and the absolute magnitude in the B band (M_B) for the population of AGN in the SXDS and GWS fields, and for a comparison sample of normal galaxies from the CDF-S field. Moreover, this CMR was analysed in the four redshift intervals $z \leq 0.5$, $0.5 < z \leq 1.0$, $1.0 < z \leq 1.5$, and $1.5 < z \leq 2.0$ as shown in Fig. 11. Rest-frame colours of normal galaxies were obtained from the CDF-S catalogue (Wolf et al. 2001, 2004, 2008), while for the sample of AGN the rest-frame colours and the absolute magnitudes were computed from the k-corrected apparent magnitudes. The population of normal galaxies shows the aforementioned bimodality of colours at all observed redshifts. We plotted on all diagrams the Melbourne et al. (2007) rest-frame colour separation ($B - V = 0.6$), to distinguish between galaxies belonging to the red sequence (those with $B - V > 0.6$) and the blue cloud (those with $B - V < 0.6$).

As shown in Figs. 10 and 11, we can confirm some of results found in previous works (e.g., Nandra et al. 2007; Georgakakis et al. 2008; Silverman et al. 2008; Schawinski et al. 2009): most

[19] Classifying Objects by Medium-Band Observations – a spectrophotometric 17-filter survey; http://www.mpia.de/COMBO/combo_index.html

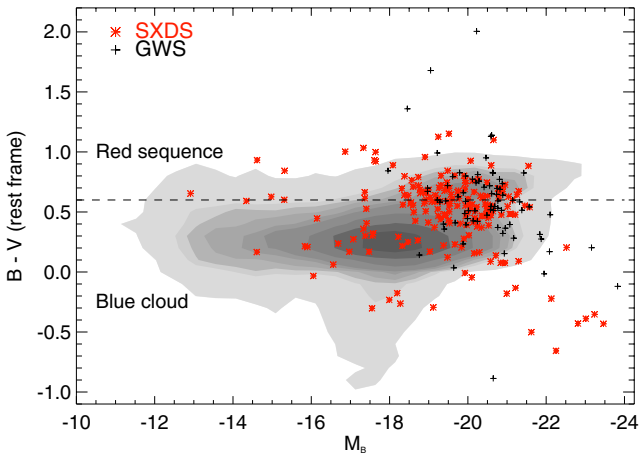

Fig. 10. Colour–magnitude diagram showing the relationship between the rest-frame $B-V$ colour and the absolute magnitude in the B band for AGN in the SXDS (red stars) and GWS (black crosses) fields with redshifts $z \leq 2$. The sample of AGN is compared with a sample of normal galaxies from the CDF-S field (Wolf et al. 2001, 2004, 2008) represented by contours. The grey scales of the contours are scaled to the data, where the darkest and brightest show the highest and the lowest density of the sources, respectively. The dashed line shows the Melbourne et al. (2007) separation between the red sequence ($B-V > 0.6$) and blue cloud ($B-V < 0.6$) galaxies. Median error bars are 0.0083, and 0.0325 for the absolute magnitude in the B band, and 0.0198, and 0.0489 for the $B-V$ rest-frame colour, in the SXDS and GWS fields, respectively.

X-ray selected AGN reside in the green valley, which is the region between the red sequence and blue cloud, located at both the bottom of the red sequence and the top of the blue cloud. At least ≈60% of the AGN in the SXDS and GWS fields are located in this region of the colour–magnitude diagram with absolute M_B magnitudes in the range $-18.0 \lesssim M_B \lesssim -21.5$ and rest-frame colours in the range $0.3 \lesssim B-V \lesssim 0.9$. If we compare the distributions of rest-frame $B-V$ colours for both red and blue AGN with those for normal galaxies, it can be seen that the distribution of red AGN peaks towards bluer colours ($B-V \approx 0.62$), while the distribution of blue AGN peaks at redder colours ($B-V \approx 0.57$) than the sample of red and blue normal galaxies ($B-V \approx 0.7$ and ≈0.3, respectively). As shown in Fig. 11, AGN start to populate the green valley at higher redshifts, namely $z > 0.5$. Analysing the number of sources in redshift bins with a width of 0.1, the maximum number of AGN was found to occur at $z \approx 0.9$.

In addition to the sources found in the green valley, where most AGN reside, a number of very luminous ($M_B \lesssim -21.5$), blue sources (rest-frame $B-V \lesssim 0.2$) lie outside the region covered by the normal galaxy population (Fig. 10). They are all very luminous X-ray sources, having luminosities $L_X \geq 10^{44}$ erg s^{-1} in the 0.5–7.0 keV energy range. Moreover, practically all of these sources were classified as compact (see Sect. 4.2 for more details). This region corresponds to QSO objects. Around 10% of the total sample of the AGN studied in this work reside in this area. They start to populate the colour–magnitude diagrams at higher redshifts ($z > 1$), as shown in Fig. 11.

In comparison with previous works, we detected a much larger population of low-luminosity AGN ($M_B \gtrsim -18.0$), most of them at redshifts <1.0, which are located in both the blue cloud and red sequence. Around 15% of the AGN in the whole sample were found to lie in this region. These AGN can occupy a wide range of rest-frame colours ($-0.4 \lesssim B-V \lesssim 1.1$), with most of them having X-ray luminosities above 10^{43} erg s^{-1} in the 0.5–7.0 keV energy range. All these objects belong to the SXDS field and weren detected for the first time thanks to the considerable depth of the optical data.

As already shown, it seems that the colours of X-ray detected active galaxies differ from those of non-active galaxies, at all observed redshift intervals. Normal galaxies show clear bimodality at all redshifts, owing to galaxies belonging to the red sequence or blue cloud, while no colour bimodality has been found for AGN. Galaxies residing in the green valley are usually considered to be transition sources, transforming from blue, star-forming galaxies to red, passively-evolving early-type objects. Therefore, since most AGN have been found to be located in this region, it has been suggested in several previous works that there is a relationship between the aforementioned transition and AGN activity, and that AGN feedback might be responsible for quenching the star formation in blue cloud galaxies and transforming into earlier types (e.g., Nandra et al. 2007; Georgakakis et al. 2008; Silverman et al. 2008; Treister et al. 2009; Springel et al. 2005; Schawinski et al. 2006; Hasinger 2008).

However, a few considerations should be made when comparing the colours of normal and active galaxies:

- *Completeness limit of the comparison galaxies.* We verified the completeness limits of both the AGN and control samples, finding that ∼20% of AGN (≈22% and ≈17% in the B band and V band, respectively) have magnitudes brighter than the completeness limit of the comparison non-active galaxies, which is too small a population to alter our general conclusions about the AGN distribution in the colour–magnitude diagrams.
- *AGN contribution.* The AGN contribution to the host galaxy emission has not been quantified in this work. It has been analysed by other authors, who have found evidence that the galaxies hosting AGN with low X-ray luminosities ($\log L_X \lesssim 44$), which are mostly located in the green valley, should have even redder colours after the AGN contribution is eliminated and the total galaxy light is flux-corrected (Kauffmann et al. 2007; Nandra et al. 2007; Silverman et al. 2008). Using HST images, Cardamone et al. (2010) studied how the light from the central nuclear source affects the colours of moderate-luminosity AGN host galaxies in the GOODS survey. They found that the integrated optical galaxy light is dominated by host emission, and that optical colours are insignificantly affected by AGN emission. Moreover, Pierce et al. (2010) found that only fewer than some 10% (when the AGN is very luminous, unobscured, and/or compact) of X-ray selected AGN can significantly affect the integrated optical and UV colours of their host galaxies; otherwise, the AGN contribution to the integrated optical/UV colours is insignificant.
- *Dust reddening.* In several previous works, it has been found that many blue, star-forming galaxies reddened by dust have colours that would place them in the green valley. This could mean that many green-valley galaxies are not transition sources, evolving from blue to passively-evolving red galaxies, but rather blue cloud sources affected by dust. Moreover, a selection effect could be responsible whereby AGN less affected by extinction are more likely to be observed, and the most reddened AGN might than have magnitudes fainter than the detection limits. Using NIR colours to distinguish between the red early-type galaxies and galaxies being reddened by dust (at $0.8 \leq z \leq 1.2$), Cardamone et al. (2010) found that ∼25% and ∼75% of AGN belonging to

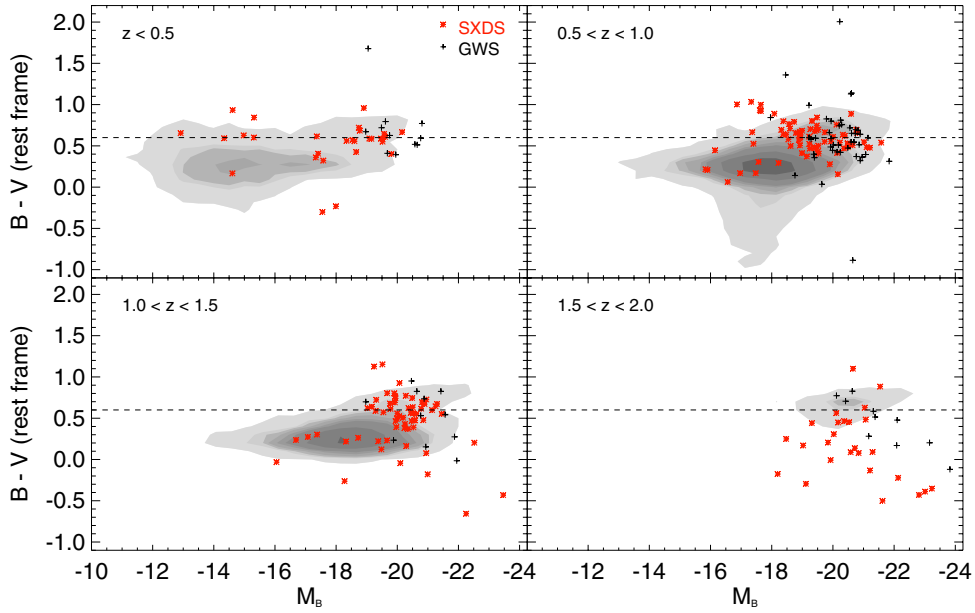

Fig. 11. The same colour–magnitude diagram as shown in Fig. 10, but presented in four redshift intervals, from up to down, and from left to right: $z \leq 0.5$, $0.5 < z \leq 1.0$, $1.0 < z \leq 1.5$, and $1.5 < z \leq 2.0$.

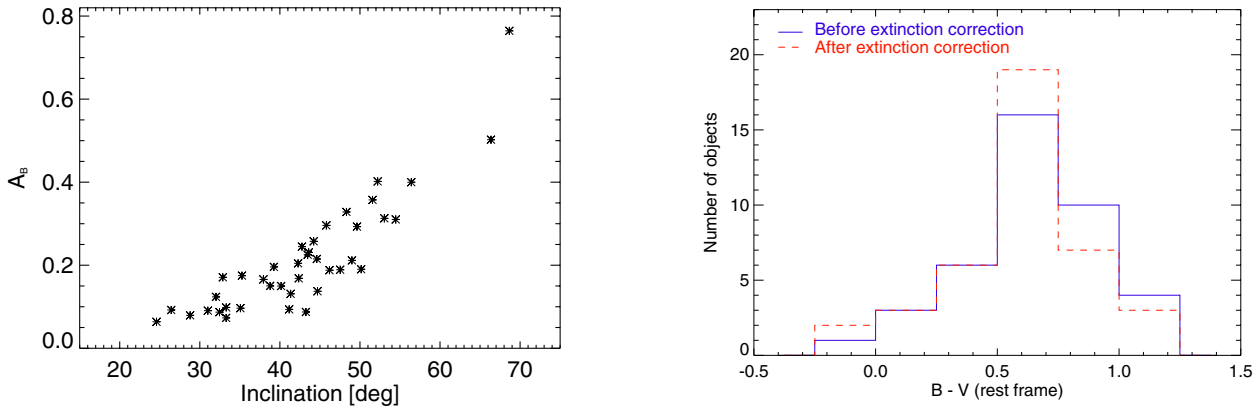

Fig. 12. *Left*: relationship between the extinction A_B measured in B band and inclination for late-type AGN host galaxies in the SXDS field. *Right*: histogram showing the distribution of $B-V$ colour before (solid blue line) and after (dashed red line) extinction correction for late-type AGN host galaxies selected in the SXDS field.

the red sequence and green valley, respectively, actually have colours typical of young stellar populations being reddened by dust, and that their dust-corrected optical colours are blue and similar to those of star-forming galaxies. However, using dust-corrected optical colours, Xue et al. (2010) found a very weak colour bimodality for AGN host galaxies at redshifts $z \leq 1.0$, and no evidence of this at higher redshifts, suggesting that even after dust-correction active galaxies still appear redder than non-active galaxies, at all redshifts. We studied the effect of dust-reddening in our sample of late-type AGN selected in the SXDS field. To measure the extinction in both B and V bands, and the extinction corrected rest-frame $B-V$ colour, we used the same corrections as in Fernández Lorenzo et al. (2010). As noted in that paper, using the Tully et al. (1998) method the extinction A_B in the B band can be measured as a function of the inclination i, in terms of major-to-minor axis ratio a/b $A_B = \gamma_B \log(a/b)$, where $\gamma_B = -0.35\,(15.31 + M_B)$. These formulae were derived using a sample of spiral galaxies and the Vega magnitudes. Therefore, we considered Vega magnitudes when analysing the extinction correction, studying only galaxies classified as late-types. The major and minor axes were obtained using SExtractor. As noted by Fernández Lorenzo et al. (2010), using Calzetti et al. (2000) the extinction in the V band can be calculated as $A_V = 0.8\,A_B$. Figure 12 (left panel) shows the relationship between the inclination and the obtained extinction in the B band. After applying the extinction corrections, we did not find any significant difference in the colour distribution of late-type AGN. Figure 12 (right panel) compares the $B-V$ colour before and after applying the extinction correction. Moreover, by performing a Kolmogorov-Smirnov analysis, we obtained a significance level of 0.72, indicating

that the cumulative distribution functions of $B-V$ colour before and after applying the extinction correction do not significantly differ. This would mean that even after the extinction correction, the late-type galaxies, which should be more affected by dust reddening than early-types, remain mainly in the green valley. However, the extinction correction applied here is only a coarse one, since the equations used were derived for the local universe, and no corrections related to the possible evolution of dust content with the redshift were applied.

In contrast, other results show that when comparing samples of active and normal galaxies with similar stellar masses and at similar redshifts, AGN host galaxies do not appear to display either quenched or elevated star formation (e.g., Alonso-Herrero et al. 2008). Moreover, studying the CMRs of X-ray selected active and non-active galaxies at high redshifts $z \approx 1{-}4$, Xue et al. (2010) found a colour bimodality in non-active galaxies that is absent in AGN hosts. This holds up to $z \approx 1{-}3$ (in good agreement with the results mentioned above). Nevertheless, using stellar mass-selected samples they found that the difference between the colour distributions of active and non-active galaxies disappears, and that mass-selected AGN hosts have the same bimodal distributions in the CMRs as non-active galaxies, up to $z \approx 2{-}3$. The authors suggested that AGN preferentially reside in massive galaxies that normally tend to have redder colours. However, these results disagree with those of Schawinski et al. (2010) in the nearby universe, where the colours of mass-selected AGN still peak in the green valley.

We measured the stellar masses of our active galaxies (from both the SXDS and Groth fields) and galaxies in the control sample using the same procedure as Xue et al. (2010). Figure 13 shows the relationship between the stellar mass in B band and the rest-frame $B-V$ colour. For a sample of AGN studied in this work, even when mass-matched with a sample of inactive galaxies, we do not find any clear colour bi-modality. Around 60% of the AGN in our sample reside between the red sequence and blue cloud, having stellar masses between $10^{9.7}$ and $10^{11}\ M_{\odot}$. This is a similar population to that found residing in the green valley of colour–magnitude diagrams (see Fig. 10). However, in comparison with Xue et al. (2010), we have analysed different stellar mass populations, which have a smaller fraction of galaxies at redshifts between 1.0 and 2.0, and no examples of the most massive galaxies (above $10^{11}\ M_{\odot}$) that they found residing on the red sequence.

4.2. CMRs in relation to morphology

As mentioned above, CMRs have been used in previous studies as a means of assessing the role of both AGN activity and AGN feedback in galaxy evolution (e.g., Nandra et al. 2007; Georgakakis et al. 2008; Silverman et al. 2008; Schawinski et al. 2009). In previous works, this type of analysis has usually been performed using a whole population of AGN. To understand the role of AGN in galaxy evolution, it is necessary to study the colour–magnitude diagrams of different morphological types (instead of the whole population), at both low and high redshifts. This paper is one of the first to analyse CMRs in terms of morphology using a high-redshift (up to $z = 2$) magnitude-limited AGN sample.

Figure 14 shows the CMRs of X-ray selected AGN in the SXDS and GWS fields, taking into account the morphological classification of sources. Colour–magnitude diagrams are presented for both compact sources and the two main

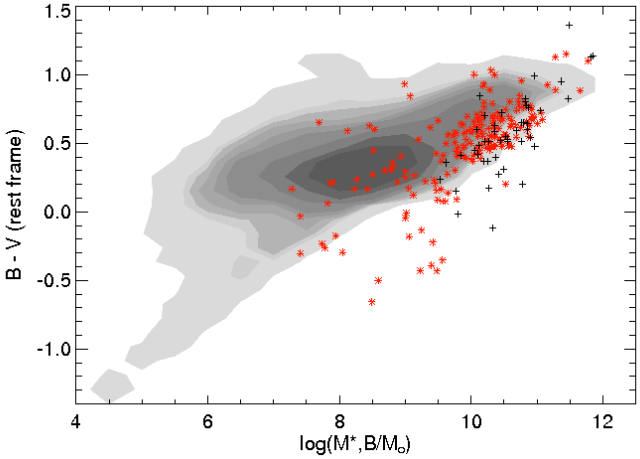

Fig. 13. Relation between the rest-frame $B-V$ colour and the stellar mass in the B band for a sample of AGN in the SXDS (red stars) and GWS (black crosses) fields having redshifts $z \leq 2$. See Fig. 10 for a description of a control CDFS sample represented with grey contours.

morphological types of early- and late-type AGN host galaxies. We have plotted data for all AGN with redshifts $z \leq 2.0$. The morphological classification of active galaxies belonging to the SXDS field has been described in Sect. 3. For the selection and morphological classification of AGN in the GWS field, we refer to Pović et al. (2009a). Groups classified as I and II in Pović et al. (2009a) have been presented here as early- and groups III and IV as late-type galaxies. As in Figs. 10 and 11, for each morphological type the distribution of active galaxies has been compared with the distribution of the global population of normal galaxies from the CDF-S field.

As can be seen in Fig. 14, more than 85% of the sources classified as compact have blue colours, with many of them residing in the green valley. A significant number of these sources are QSOs, but AGN with faint hosts and spheroidal galaxies are also present. Around 25% of the compact sources reside in the region devoid of normal galaxies, with very blue colours and high luminosities typical of high redshift QSOs.

On the other hand, no clear separation has been found between early- and late-type galaxy hosts on the colour–magnitude diagrams. Both types seem to follow a similar distribution, being again mostly located in the green valley, at the bottom of the red sequence, and at the top of the blue cloud. Therefore, the AGN analysed in this work do not show a clear relationship between the colours and morphology. On the other hand, the colours of active galaxies can be influenced by AGN and/or dust obscuration, moving the early-/late-type sources toward the blue cloud/red sequence, respectively. However, as already noted in Sect. 4.1, we still need to quantify these contributions.

This is one of the first papers in which AGN colour–magnitude relations have been studied according to morphology, for AGN at $z \leq 2$. Schawinski et al. (2010) studied colour-stellar mass diagrams (instead of colour–magnitude relations) but in the nearby universe ($z < 0.05$) for early- and late-type AGN host galaxies. In these diagrams, they did not find a relationship between colours and morphology, for either the largest population of AGN in the green valley with early-type AGN hosts fainter than the red sequence, or the population of AGN in late-type galaxies that peaks in the green valley, above the blue cloud population of similar masses. Moreover, Mainieri et al. (2011) studied the colours and morphology of type-2 QSO at redshifts between 0.8 and 3 in the XMM-COSMOS field, finding that most

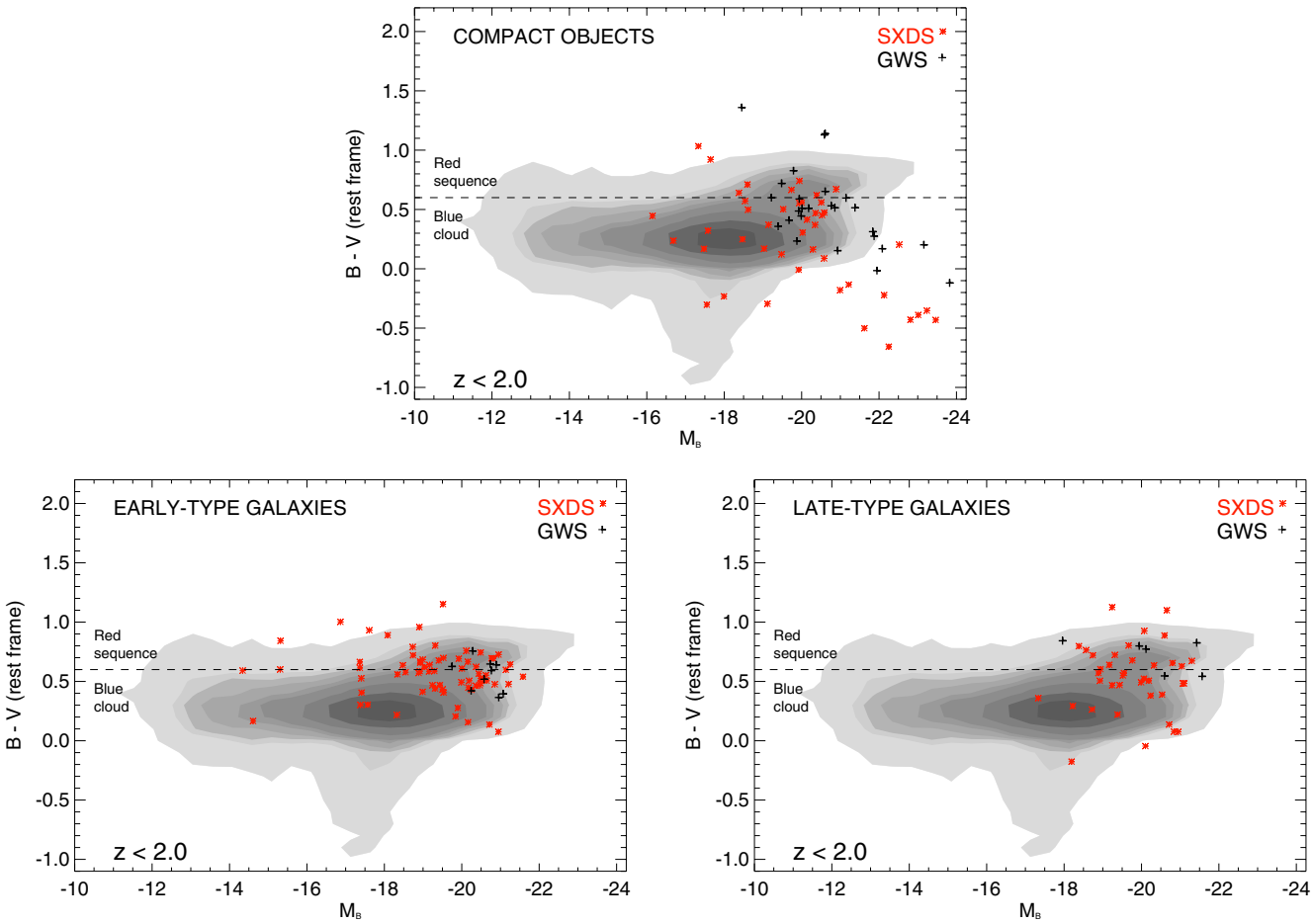

Fig. 14. Colour–magnitude diagram showing the relationship between the rest-frame $B - V$ colour and the absolute magnitude in the B band for different morphological types, using a sample of X-ray selected AGN in the SXDS (red stars) and GWS (black crosses) fields. All AGN having redshifts $z \leq 2.0$ are presented, compact (*top*), early- (*bottom left*) and late-type (*bottom right*) galaxy hosts. Morphological classification of active galaxies in the SXDS field is described in Sect. 3, while morphological classification of active galaxies in the GWS field is described in Pović et al. (2009a). The sample of AGN is compared with the sample of normal galaxies in the CDF-S field (Wolf et al. 2001, 2004, 2008) represented with contours. Grey scales of the contours are scaled to the data, where the darkest and brightest show the highest and the lowest density of the sources, respectively. The dashed line shows the Melbourne et al. (2007) separation between the galaxies belonging to the red sequence ($B - V > 0.6$) or to the blue cloud ($B - V < 0.6$).

of their objects have rest-frame colours in the green valley, and attributing this to the effect of a luminosity-selected rather than a mass-selected sample. More than 80% of their objects have stellar masses above $10^{10}\,M_{\odot}$, mostly showing bulge-dominated morphologies, and weak signs of recent mergers or discs.

4.3. CMRs in relationship with X-ray type

To study the colour–magnitude diagrams in terms of X-ray obscuration, we performed a coarse nuclear-type classification based on a diagnostic diagram relating the X/O flux ratio to the hardness ratio HR(2–4.5 keV/0.5–2 keV). The X/O flux ratio has been shown to differentiate efficiently between active and non-active/Compton-thick galaxies (Alexander et al. 2001; Fiore et al. 2003; Civano et al. 2007), while the hardness ratio HR(2–4.5 keV/0.5–2 keV) was found to be very sensitive to absorption, thus capable of disentangling X-ray type-1 (unobscured or unabsorbed) from X-ray type-2 (obscured or absorbed) AGN (Mainieri et al. 2002; Della Ceca et al. 2004; Perola et al. 2004; Caccianiga et al. 2004; Dwelly et al. 2005; Hasinger 2008). Full details of the methodology that we applied in the present paper are given in Pović et al. (2009a). On the basis of this, all objects having $X/O > 0.1$ and HR(2–4.5 keV/0.5–2 keV) < -0.35 were classified as X-ray type-1 AGN, while those with $X/O > 0.1$ and HR(2–4.5 keV/0.5–2 keV) > -0.35 were catalogued as type-2 (obscured) nuclei. Those with $X/O < 0.1$ were classified as Compton-thick/non-active galaxies. Figure 15 shows the corresponding diagram of X-ray type classification. A fraction of 52% and 39% of the sources with optical counterparts were classified as X-ray type-1 and type-2 AGN, respectively. The dashed–line box indicates the locus of the X-ray type-1 region according to Della Ceca et al. (2004). This box was considered as the "highest probability" region for finding X-ray unobscured AGN, and is populated by 51% of the X-ray type-1 objects. The remaining 10% are found in the region typical of Compton-thick/non-active galaxies.

Using our complete sample of objects, we studied the relationship between the $B - V$ rest-frame colour and the HR(2–4.5 keV/0.5–2 keV) hardness ratio. Both X-ray type-1 and X-ray type-2 sources span the same range of $B - V$ colour, and there is apparently no relationship between the observed optical and X-ray colours when the complete population of AGN is considered. However, performing the Kolmogorov-Smirnov

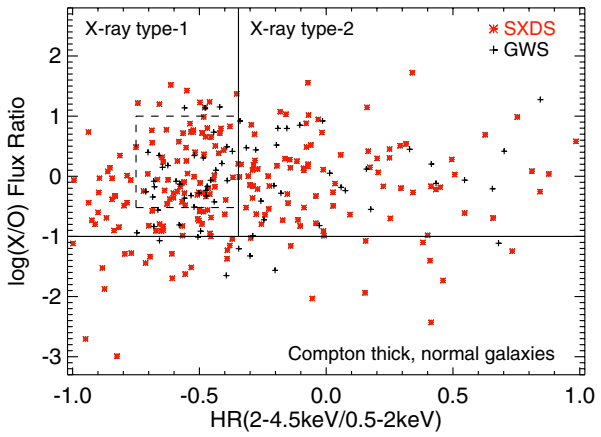

Fig. 15. Relationship between the X/O flux ratio and HR(2−4.5 keV/0.5−2 keV) hardness ratio, for X-ray emitters with optical counterparts in the SXDS (red stars) and GWS (black crosses) fields. Solid lines separate X-ray type-1 (unobscured) from both the X-ray type-2 (obscured) regions and the area with $X/O < 0.1$, where Compton thick AGN, normal galaxies, and stars can be found (e.g. Fiore et al. 2003). The dashed line box shows the limits obtained by Della Ceca et al. (2004), where ∼85% of their spectroscopically identified AGN with broad emission lines have been found. In this work, ∼51% of the X-ray type-1 sources are located inside this box.

analysis produces the result that the two distributions might be different, although the evidence is inconclusive, having a probability factor of 0.3.

Figure 16 shows the CMRs in terms of the X-ray obscuration. X-ray type-1 and type-2 sources have been represented from both the SXDS and GWS fields, and compared with the distribution of the complete sample of normal galaxies from the CDF-S field. As can be seen, there is no clear distinction between X-ray unobscured and obscured sources in the colour–magnitude diagram. We studied this diagram in four redshift intervals (same intervals as in Fig. 11), and found no clear distinction between X-ray type-1 and type-2 sources in any of them. We studied the X-ray obscuration for each morphological type of our analysed sample. Almost all active galaxies (95%) detected as compact are unobscured sources in X-rays, with most of them (more than 80%) having blue $B - V$ rest-frame colours. High luminosity QSO sources, which occupy a region devoid of normal galaxies, are found to be the most unobscured sources, having HR(2−4.5 keV/0.5−2 keV) < –0.5, while compared with them, compact sources belonging to the green valley and the blue cloud have lower X-ray obscurations (–0.5 ≤ HR(2−4.5 keV/0.5−2 keV) ≤ –0.36). On the other hand, when considering early- and late-type active galaxies, no relation has been found between the morphology and X-ray obscuration. Early- and late-type AGN in our sample of AGN host galaxies consist of a mixture of both X-ray unobscured and obscured sources. For both morphological types, ≈55% of sources are unobscured, while the remaining ≈45% are obscured. Moreover, there is no significant relationship between the X-ray obscuration and optical $B - V$ rest-frame colour for both morphological types. We found 55% and 50% of unobscured and obscured early-type AGN to have blue optical colours, respectively, with very similar values for late-type hosts (58% and 50%). However, early-type galaxies that reside in the blue cloud are found to be more unobscured in X-rays (−0.8 ≲ HR(2−4.5 keV/0.5−2 keV) ≲ –0.5) than those belonging to the green valley (HR(2−4.5 keV/0.5−2 keV) > –0.5). This suggests that part of the X-ray obscuration is caused by the

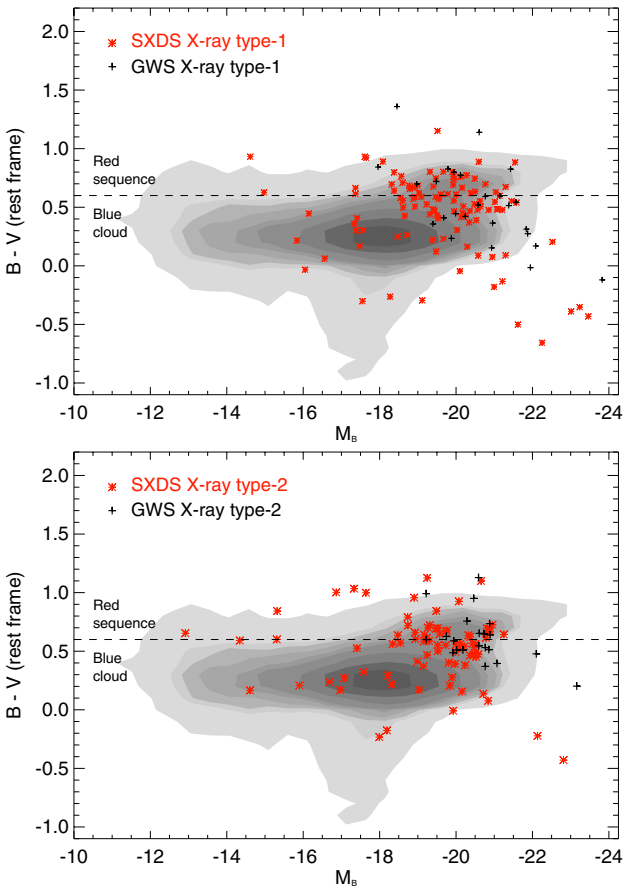

Fig. 16. Colour–magnitude diagram showing the relation between the rest-frame $B - V$ colour and the absolute magnitude in the B band for X-ray type-1 (unobscured; *top*) and X-ray type-2 (obscured; *bottom*) AGN, selected in the SXDS (red stars) and GWS (black crosses) fields. All sources with redshifts $z \leq 2.0$ have been represented. AGN sample has been compared with the sample of normal galaxies selected in the CDF-S field (Wolf et al. 2001, 2004, 2008) represented with contours. The grey scales of the contours are scaled to the data, where the darkest and brightest show the highest and the lowest density of the sources, respectively. The dashed line shows the Melbourne et al. (2007) separation between the galaxies belonging to the red sequence ($B - V > 0.6$) or to the blue cloud ($B - V < 0.6$).

galaxy itself, moving the host-galaxy colours from those of the blue cloud to the red sequence. X-ray obscured early-type galaxies cover a wide range of hardness ratios (up to 1.0), with those sources belonging to the blue cloud and green valley having slightly lower obscuration than objects located in the red sequence. On the other hand, X-ray unobscured late-type sources seem to be more obscured than unobscured early-types, while for X-ray obscured late-types obscuration seems to be similar to that of obscured early-type galaxies.

Recently, Pierce et al. (2010) searched for correlations between both the nuclear and outer $U - B$ colours and X-ray obscuration, which was defined in terms of the hardness ratio HR(2− 7keV/0.5−2 keV), using a sample of X-ray selected AGN in the AEGIS field at redshifts $0.2 < z < 1.2$. For most of their objects selected as X-ray type-1 AGN, they obtained bluer colours, while they found that X-ray type-2 sources hosts are characterised by redder colours. As shown in Fig. 16, no clear identification of such a type of sources was found between the $B - V$ colour and the HR(2−4.5 keV/0.5−2 keV) hardness ratio used in this work, when the complete population of AGN is observed. However, when we attempt to distinguish between

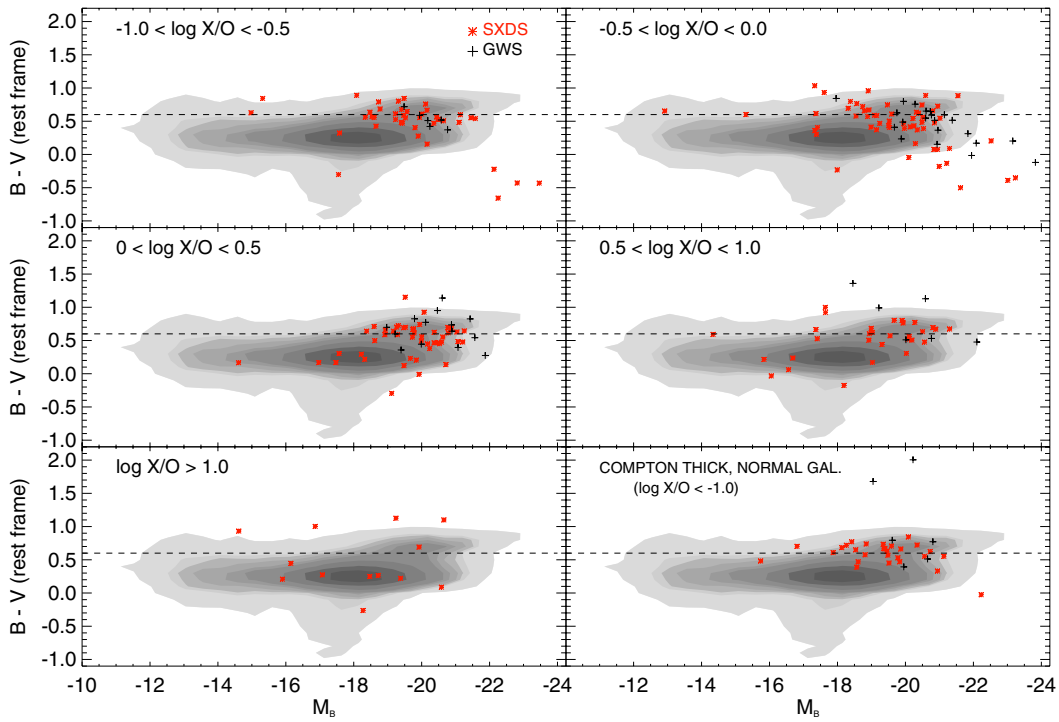

Fig. 17. Colour–magnitude diagram showing the relationship between the rest-frame $B-V$ colour and the absolute magnitude in the B band for AGN in the SXDS (stars) and GWS (crosses) fields having different X-ray-to-optical flux ratio. All sources have redshifts $z \leq 2.0$. The sample of AGN is compared with the sample of normal galaxies in the CDF-S field (Wolf et al. 2001, 2004, 2008) represented with contours. Grey scales of the contours are scaled to the data, where the darkest and brightest show the highest and the lowest density of the sources, respectively. The dashed line shows the Melbourne et al. (2007) limit between galaxies belonging to the red sequence ($B-V > 0.6$) and those in the blue cloud ($B-V < 0.6$). The bottom right diagram shows the distribution of objects classified as non-AGN (Compton thick and normal galaxies), having very low values of the X/O flux ratio.

different morphological types in terms of X-ray obscuration for, it seems that there might be a weak correlation between X-ray and optical colours.

4.4. CMRs in terms of X/O flux ratio

Finally, we studied the CMRs in terms of the X-ray-to-optical (X/O) flux ratio. The physical explanation of this parameter is still not evident, but as suggested in Pović et al. (2009b) it might be related to the accretion rate. Studying X-ray properties, such as the X/O flux ratio and X-ray luminosities, we can test the black hole growth rate in relationship to the properties of host galaxies, colours, and morphology.

Figure 17 shows the CMRs according to the X/O flux ratio. We studied the distribution of AGN analysed in this work, considering five ranges of X/O flux ratio. We also analysed the distribution of objects with very low X/O flux ratios ($\log X/O < -1$) characteristic of Compton thick sources and/or normal galaxies (e.g., Alexander et al. 2001; Fiore et al. 2003; Civano et al. 2007). As can be seen, most of these objects also reside in the green valley, having colours that correspond to most AGN sources.

Examining Fig. 17, we found that the distribution of AGN sources moves across the colour–magnitude diagram as the X/O flux ratio changes. Objects having higher values of the X/O flux ratio (e.g. $\log X/O > 0.5$) have bluer colours, while most AGN with lower X/O flux ratios have red and green colours with respect to that of normal galaxies. This might be related to two scenarios. First, that AGN with higher X/O flux ratios, have younger stellar populations, hence bluer optical colours. If X/O flux ratio is a parameter proportional to the Eddington ratio, as suggested by Pović et al. (2009b), and higher accretion rates and stronger AGN activity provoke a stronger AGN feedback, AGN feedback may not quench the star formation, unless we observe the initial phases when star-formation quenching is just beginning. And second, for very high Eddington ratios, AGN do contribute to the optical colours of their host galaxies, making them bluer. We also note that all sources located in the region not covered by normal galaxies, being very blue, very luminous, and probably high redshift QSO sources, have lower values of the X/O flux ratio ($\approx \log X/O \leq 0$). Although the analysed sample of AGN seems to be representative of a full X-ray population as shown in Sect. 2.7, we should be aware that the observed trends represent just a small fraction of the full X-ray population.

Figure 18 shows the normalised distributions of X/O flux ratio for the early- and late-type galaxies, and for the X-ray unobscured and obscured sources of the sample analysed in this paper (see Sect. 2.7) and of all optical counterparts. It can be seen that high values of the X/O flux ratio ($X/O > 0.5$) correspond to AGN hosted by later-types. This result was previously obtained by Pović et al. (2009b), suggesting that late-type AGN, having more material to feed the black hole, have higher Eddington ratios than with early-type AGN. Mainieri et al. (2011) obtained the same result for type-2 QSOs, where disk-dominated or merging systems in their sample have higher accreting rates than bulge-dominated galaxies. Moreover, we compared the X-ray luminosities in three energy ranges, soft, hard, and veryhard (see Table 1) for early- and late-type active galaxies, as can be seen in Fig. 19. Performing the Kolmogorov-Smirnov test, it was found that the distributions in the three ranges differ significantly different in hard and veryhard X-rays with probability factors of

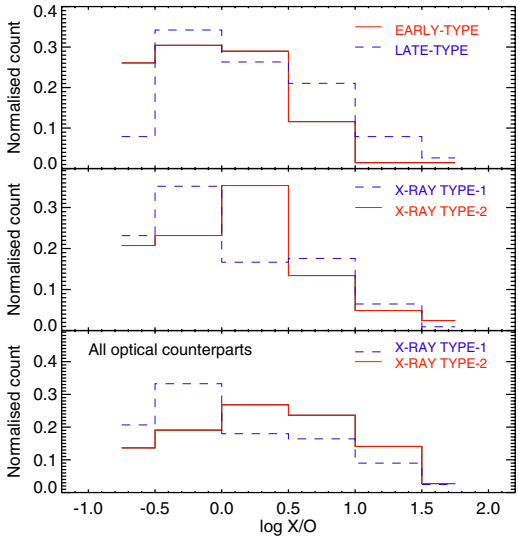

Fig. 18. Normalised X/O flux ratio distributions. (*Top*) Two main morphological types, early- (solid red line) and late-type (dashed blue line) active galaxies, are presented. The other two panels represent X-ray type-1 (dashed blue line) and type-2 (solid red line) sources of a sample analysed in this paper (*middle*) and of all optical counterparts (*bottom*).

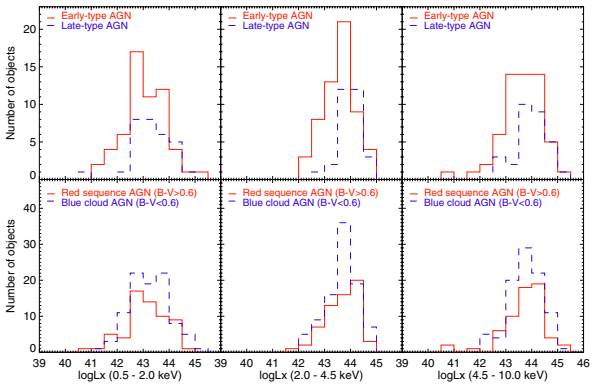

Fig. 19. *From left to right*: histogram showing a distribution of X-ray luminosities in three energy ranges: soft (0.5–2.0 keV), hard-2 (2.0–4.5 keV), and very hard (4.5–10.0 keV). *Top:* early- (solid red line) and late-type (dashed blue line) active galaxies are presented. *Bottom:* red (solid red line) and blue (dashed blue line) AGN, having $B-V$ colours >0.6 and <0.6, respectively, are presented.

only 0.0004 and 0.025 that they belong to the same parent distribution. It can again be seen that AGN hosted by later-types have higher X-ray activities than early-types. On the other hand, when we analyse X-ray luminosities with respect to the $B-V$ colour, dividing all sources into red ($B-V > 0.6$) and blue ($B-V < 0.6$) active galaxies, the Kolmogorov-Smirnov analysis suggests that their X-ray activities do not differ significantly, with probabilities of 93%, 68%, and 81% in three energy ranges, respectively, and that they belong to the same parent distribution.

Finally, we compared the normalised distributions of X/O flux ratios for X-ray type-1 and type-2 AGN of a sample analysed in this paper (middle panel) and all optical counterparts (bottom panel). We found similar distributions between two samples, where lower values of the X/O flux ratio (<0) are more populated by X-ray unobscured AGN.

4.5. Summary: our results and current models of AGN formation and evolution

As shown in Fig. 10, and analysed above, AGN hosts seem to have different colours than normal galaxies, with the peak of red/blue AGN host galaxies being moved to bluer/redder colours, respectively. As mentioned in Sect. 4.2, to more clearly understand what we see on the colour–magnitude diagrams and relate the results obtained to existing models of AGN formation and evolution, it is necessary to study colour–magnitude relations in more detail. In addition, instead of observing whole populations of active galaxies, we need to observe different morphological and nuclear types. As we have seen, almost all AGN classified as compact objects (which are possible QSO sources) are found to be X-ray unobscured and blue galaxies. However, when observing the two main morphological types, early- (which seem to be the majority of X-ray detected AGN) and late-type galaxies, no relationship was found between colours and morphology, showing that early-/late-type X-ray selected AGN are not necessarily as red/blue as non-active galaxies, respectively. To explain the presence of similar ("green") colours for both morphological types located in the green valley, there are two possibilities:

1) *Early- and late-type X-ray detected AGN have different stellar populations, which are similar to those of normal galaxies belonging to the red sequence and blue cloud, respectively*. In this case, two mechanisms might be responsible for the different colours of AGN: AGN contribution to total galaxy light, affecting more early-types and making them bluer, and dust reddening, affecting most of all late-types and making them redder. However, we still lack proof of this scenario. As shown in Sect. 4.1, the AGN contribution to optical colours has been shown to be negligible in most (if not all) previous analyses (Kauffmann et al. 2007; Nandra et al. 2007; Silverman et al. 2008; Cardamone et al. 2010), for at least 90% of AGN (Pierce et al. 2010). Moreover, we have seen that it is still unclear how great the influence of the dust reddening could be on the optical colours (Cardamone et al. 2010; Xue et al. 2010). However, even if the dust-reddening effect is significant (moving later-types to bluer colours after extinction correction), since most AGN reside in early-type systems (which are less affected by dust), after extinction correction most AGN might still reside in the green valley, without showing the colour bimodality typical of non-active galaxies.
2) *Early- and late-type X-ray detected AGN have similar stellar populations, which are different from those of normal galaxies belonging to the red sequence and blue cloud, respectively*. AGN might be hosted by similar galaxies, both later early- and earlier late-type sources, representing collectively one phase in the evolution of galaxies. Moreover, in the redshift intervals studied in this work (see Fig. 11), we have seen that most green-valley AGN are found at redshifts $0.5 \leq z \leq 1.5$. This possibility supports the hypothesis that green-valley AGN are transition objects, between the blue starburst galaxies and red, massive ellipticals, as proposed by various authors (e.g., Springel et al. 2005; Schawinski et al. 2006; Nandra et al. 2007; Georgakakis et al. 2008; Silverman et al. 2008; Treister et al. 2009).

We independently analysed three regions of the diagrams in terms of their absolute magnitudes, and compared the results with the current models of AGN formation and evolution. Taking into account that no clear trend has been found in the CMR's when observing different morphological, X-ray, or X/O types,

we should be careful when studying galaxy evolution. As we move from the right to the left on the colour–magnitude diagrams (from brighter to fainter B band absolute magnitudes), we may interpret what we see in CMRs (Figs. 10, 11, 14, 16, and 17) in the following way:

– *Region I*: Very bright magnitudes ($M_B < -21.0$), very blue colours. This region corresponds to the one unpopulated by normal galaxies in our colour–magnitude diagrams. All AGN have high redshifts, from 1.5 to 2.0. They are all very blue, compact, and X-ray unobscured sources, having low values of hardness ratios. We suspect that these sources are high-redshift quasars, and that the AGN are in the so-called "QSO-mode" (Hopkins et al. 2005a,b; Springel et al. 2005; Croton et al. 2006; Hopkins et al. 2008a,b). In this mode, galaxy mergers and interactions are the main mechanisms triggering nuclear activity in galaxies, providing enough material for both star formation and supermassive black hole feeding. In the beginning, the QSO is obscured by gas, but eventually it blows the obscuring and star-forming gas out from the galaxy by means of different AGN feedback mechanisms: ionisation, heating, radiation pressure (e.g., Ciotti & Ostriker 2007) and/or through strong winds and jets (e.g., Ciotti et al. 2009; Shin et al. 2010, and references therein). After that, the AGN may become unobscured, and the light coming from the nuclear region dominate the light coming from the host galaxy.

– *Region II*: From intermediate to bright magnitudes ($-21.0 < M_B < -18.0$), green colours. This is the region where >60% of the AGN from our sample are located, being mostly concentrated in the green valley, at the end of the blue cloud and bottom of the red sequence. As already mentioned and shown, the majority of X-ray detected AGN populate this region at redshifts $0.5 \leq z \leq 1.5$, showing different levels of nuclear activity (wide range of X/O flux ratio). The region is populated by compact sources, being again mostly unobscured and blue, but also by early- and late-type active galaxies, although AGN hosted by early-types are more numerous, as shown in Sect. 3. They have similar colours, and have similar levels of X-ray obscuration, being both unobscured and obscured in X-rays. It is possible that at these redshifts we observe one of the peaks of nuclear activity in the evolution of galaxies (e.g., Hasinger et al. 2005), related to the peak of starburst activity, with a possible dynamical delay (Davies et al. 2007a; Schawinski et al. 2009; Wild et al. 2010; Hopkins 2011). To explain the properties of the AGN observed in this region and in the redshift range considered, we apparently need to consider that different mechanisms are responsible for AGN fuelling. They include major and minor mergers (e.g., Surace et al. 2000; Springel et al. 2005; Di Matteo et al. 2005; Hopkins et al. 2005a,b; Cox et al. 2008; Hopkins et al. 2008a,b; Somerville et al. 2008), but also some secular mechanisms, such as minor interactions, disk instabilities, nuclear and large scale bars, colliding clouds, and supernovae explosions (e.g., Kormendy & Kennicutt 2004; Wada 2004; Hopkins & Hernquist 2009; Cisternas et al. 2011). Thus, it is not strange that most of the AGN we observe are hosted by early-type galaxies, being triggered through major/minor mergers. On the other hand, late-type AGN were probably triggered by some secular mechanisms, although it has been shown that in some cases discs can survive major mergers (Springel & Hernquist 2005; Robertson et al 2006; Governato et al. 2009). Therefore, what we are observing in this region are probably again AGN in the "QSO-mode" (objects classified as compact), and phases of AGN activity before and after the "QSO-mode", that we see as obscured and unobscured early- and late-type AGN, respectively, triggered as suggested above. An additional possibility for triggering at these redshifts could be also the "radio-mode" accretion (Croton et al. 2006) that is active after the bright QSO phase, as a result of the static hot halo formed around the host galaxy and the accretion of this hot gas onto a supermassive black hole. However, this mechanism is usually related to lower luminosities, and low accretion rates.

– *Region III*: Low optical magnitudes ($M_B > -18.0$), wide range of colours, from red to blue. Most AGN in this region are found at redshifts $z \leq 1.0$. Around 30% of sources are compact, being normally blue and unobscured, while the remaining objects have been classified as early- or late-type galaxies, both unobscured and obscured in X-rays. What we observe in this region could be, on the one hand post "QSO-mode" AGN, that we see as unobscured early- and late-type AGN, triggered by some of the mechanisms described above, including AGN with the "radio-mode" accretion, and on the other hand newly triggered AGN, at these redshifts probably by some secular mechanisms (Cisternas et al. 2011, and references therein).

5. Conclusions

The main objective of this work has been to study the connection between the AGN and the host galaxy, in order to derive clues for understanding some of the still unanswered fundamental questions related to the AGN fuelling mechanisms, and their formation and evolution. To achieve the proposed objectives, we have studied morphology and colours, two key elements for analysing the properties of the host galaxies, in relation to X-ray properties describing the AGN activity (X-ray luminosities, X-ray obscuration, X/O flux ratio). We chose to analyse data acquired for the SXDS field, observed in X-rays with *XMM-Newton*, which has one of the deepest sets of optical data. After reducing X-ray data and source detection, we derived a catalogue of 1121 X-ray emitters and cross-matched it with the publicly available optical catalogue. We created a catalogue of 806 X-ray emitters with optical counterparts, and for these sources we measured photometric redshifts and k-corrections, to derive their rest-frame colours, absolute magnitudes, and luminosities. We obtained reliable photometric redshift information for 306 sources, for which we performed the analysis of their morphology and colours. We complemented the SXDS sample by adding our previous data from the GWS fields.

The morphological classification still seems to be one of the main challenges, especially at high redshifts where obtaining reliable morphological information becomes very difficult. In this paper, we used the galSVM (Huertas-Company et al. 2008, 2009) code, one of the new methods for morphological classification, which is especially useful when dealing with high redshift sources, and with the possibility of using a range of different morphological parameters and non-linear boundaries to separate the different types. Moreover, we used SExtractor (Bertin & Arnouts 1996) in order to obtain the input parameters for galSVM execution, and the CLASS_STAR parameter, to distinguish between compact and extended sources. Using both galSVM and SExtractor, we obtained the following:

– A set of morphological parameters, including different parameters related to the concentration of the host galaxy light and its asymmetry.

– The final morphological classification differentiates all AGN between compact sources and those hosted by one of the two main morphological types, namely early- and late-type galaxies. Approximately 22% of our objects have been classified as compact sources, while ≈30% of the AGN have been estimated to be hosted by early-type and ≈18% by late-type galaxies. For about 23% of AGN, hosts were not very clearly resolved and the AGN might reside in either early- or late-type galaxies, or be experiencing possible interactions or mergers. Around 7% of AGN remained unidentified.
– Various problems, making morphological classification more difficult, have been recognised and tested in this paper. These include systematic trends of morphological parameters with source brightness, size, and redshift, low S/N ratios, and the number of parameters needed for the morphological classification. It has been seen that there is a trend of all observed morphological parameters with the apparent magnitude, size, and distance, and that parameters related to galaxy concentration (especially the comparison of the M_{20} parameter to concentration index and/or Gini parameter) instead of to asymmetry seem to be the most affected. Moreover, it has been seen that the combination of two or three parameters can not provide a reliable morphological classification, as has been done with all previous non-parametric methods, and that classification in the multi-parameter space, with the simultaneous use of different parameters and non-linear boundaries is needed.
– At redshifts $z \leq 2.0$, at least 50% of X-ray detected AGN analysed in this work are hosted by spheroids and/or bulge-dominated galaxies. However, at least 18% of AGN in our sample are hosted by late-types, suggesting that different mechanisms may be responsible for triggering the nuclear activity in galaxies.

We studied colours of X-ray selected AGN in terms of colour–magnitude relations, comparing the AGN distribution with the typical distribution of normal galaxies. First, we used all types of active galaxies to analyse their redshift distributions (until $z \leq 2.0$). Second, using a high-redshift sample, we analysed CMRs in relation to morphology for the first time, observing the distribution of active galaxies, belonging to different morphological types, on the colour–magnitude diagrams. Third, we studied the distribution of AGN on the colour–magnitude diagrams in relation to X-ray obscuration and, finally, in relation to X/O flux ratio. We conclude the following:

– Observing all types of X-ray detected AGN the highest number of sources is found to reside in the green valley, at the top of the blue cloud, and at the bottom of the red sequence, without showing any of the colour bimodality typical of normal galaxies. AGN in our sample populate this region at redshifts ≈0.5–1.5. However, a higher number of low luminosity AGN have been detected in this work, owing to the considerable depth of the optical SXDS data in comparison with the most (if not all) previous surveys. This allows us to study the colour and morphological properties of these objects and to compare them with the properties of high luminosity AGN.
– More than 85% of objects classified as compact (possible QSO sources), are found to have blue optical colours and to be unobscured in X-rays. However, when observing the two main morphological types, no correlation has been found between the colours and morphology. The AGN studied in this work do not show the standard trend of normal galaxies, where early-types, having older stellar populations, have redder colours, while late-type galaxies, being characterised with recent stellar formation have blue optical colours. The AGN contribution and dust obscuration effects may affect the colours of early-/late-type galaxies moving them toward the blue cloud/red sequence, respectively. However, additional work is still needed to quantify these contributions. On the other hand, even when mass-matched samples are used, no clear bimodality has been seen in the optical colours. Moreover, both early- and late-type AGN are found to have similar ranges of X-ray obscuration, being both unobscured and obscured in X-rays.

Our findings confirm some previous suggestions that X-ray selected AGN residing in the green valley probably represent the transition population, in which star formation is quenched and the galaxies evolve to red sequence galaxies. What we might observe in the green valley is one of the peaks of AGN activity, with major and minor mergers probably being the main triggering mechanisms, but also some of the secular mechanisms proposed to be responsible for fuelling. We have observed AGN in the "QSO-mode" (as compact, blue, and unobscured objects in X-rays) and different phases before (observing them as obscured in X-rays) and after (observing them as unobscured in X-rays) the "QSO-mode", with AGN being hosted by later early- (the majority of sources) and earlier late-type galaxies, with similar stellar populations.

We stress again that although a sample analysed in this paper seems to be representative of a full sample of X-ray population, all results presented here have been obtained for a sample of 25% of the full X-ray population in the SXDS field.

Finally, the paper provides the scientific community with a catalogue of a large sample of AGN with the X-ray and optical data obtained in this work, including final morphological classification, all derived morphological parameters, rest-frame colours, and photometric redshifts. The complete catalogue of all 1121 X-ray sources, 806 optical counterparts, and the objects analysed in this paper is available at the CDS, while the description of columns and the small example of seven objects are presented in the appendix.

Acknowledgements. We thank the anonymous referee for a detailed analysis of the paper and constructive comments. We also thank Isabel Márquez Pérez, Josefa Masegosa Gallego, Jack Sulentic, and Ascensión del Olmo Orozco for long and very useful discussions. This work was supported by the Spanish *Plan Nacional de Astronomía y Astrofísica* under grant AYA2011-29517-C03-01. J.I.G.S. acknowledges financial support from the Spanish Ministry of Science and Innovation under project AYA2008-06311-C02-02. M.P. acknowledges Junta de Andaluca and Spanish Ministry of Science and Innovation through projects PO8-TIC-03531 and AYA2010-15169. We thank the SXDS, CDF-S, and COMBO-17 teams for making their data available to the astronomical community. We acknowledge support from the Faculty of the European Space Astronomy Centre (ESAC). We thank *XMM-Newton* Helpdesk for their helpful comments during the X-ray data reduction. This research has made use of software provided by the *XMM-Newton* Science Operations Centre and Chandra X-ray Center (CXC) in the application packages SAS and CIAO, respectively. IRAF is distributed by the National Optical Astronomy Observatory, which is operated by the Association of Universities for Research in Astronomy (AURA) under cooperative agreement with the National Science Foundation. This publication makes use of data products from the Two Micron All Sky Survey, which is a joint project of the University of Massachusetts and the Infrared Processing and Analysis Center California Institute of Technology, funded by the National Aeronautics and Space Administration and the National Science Foundation.

Appendix A: The catalogue

The full catalogue of data obtained in this work is available at the CDS. The catalogue contains SXDS X-ray data for all 1121 detected objects, optical identifications for the 806 sources, and

Table A.1. Catalogue presenting morphological properties, colours, and photometric redshifts of X-ray emitters with optical counterparts in the SXDS field.

ID	RA_x	Dec_x	F_s	F_h	F_{vh}	F_{tot}	F_{vh2}	F_{tot2}
SXDS_ID	RA_0	Dec_0	R_c	R_c_err	zphot	zphot_err	MabsB	MabsB_err
$B-V$	$B-V$_err	X/O	X/O_err	HR	HR_err	Stellarity	Elong	MSB
A	C	Gini	S	M_{20}	p_1	p_2		
1	34.2059326	–4.9195004	0.3803	2.959	5.493	2.842	11.63	3.617
SXDS-iC-121387	34.20587083	–4.918922	23.745	0.012	1.89	0.09	–20.840	0.0111
0.077	0.021	0.635	0.316	0.295	0.561	0.03	1.349	26.994
0.098	0.450	0.690	0.039	–1.293	0.167	0.833		
2	34.2367325	–4.7958641	5.128	18.22	17.888	20.502	38.996	25.817
SXDS-iC-1616	34.23629167	–4.796003	22.373	0.004	0.615	0.004	–19.264	0.003
0.701	0.0150	1.255	0.198	–0.089	0.131	0.04	1.178	24.827
0.072	0.488	0.757	0.052	–1.964	0.703	0.297		
3	34.3014336	–4.8216581	1.458	2.807	5.575	5.763	12.206	7.190
SXDS-iC-157690	34.30122083	–4.821953	24.704	0.021	1.02	0.01	–19.291	0.009
0.588	0.047	1.960	0.904	–0.163	0.406	0.58	1.829	26.736
0.093	0.449	0.719	0.063	–1.664	0.908	0.092		
4	34.3149796	–5.0099578	2.910	2.602	2.188	6.941	0.0	8.819
SXDS-iC-086715	34.31469167	–5.010572	22.232	0.003	1.42	0.01	–22.251	0.005
–0.657	0.009	0.260	0.077	–0.499	0.228	0.97	1.071	25.493
0.120	0.538	0.822	–0.0	–1.523	0.989	0.011		
5	34.3232346	–4.9310899	1.083	4.228	2.751	3.707	8.398	5.0123
SXDS-iC-115045	34.3228583	–4.931603	21.780	0.003	0.845	0.007	–20.484	0.003
0.5301	0.007	0.165	0.0544	–0.041	0.292	0.03	1.325	25.331
–0.005	0.501	0.760	–0.153	–1.919	0.711	0.289		

Notes. In the full version of the table available at the CDS, each object is represented in one line.

measured morphological parameters, final morphological classification, redshifts, and rest-frame colours for 306 X-ray emitters with optical counterparts described in Sect. 2.7. Table A.1 shows an example of the format and content of the catalogue. The column entries are as follows:

Column 1 (ID): Identification number.

Columns 2 and 3 (RA_x, Dec_x): Equinox J2000.0 right ascension and declination in degrees of the centroid in the X-ray catalogue.

Column 4 (F_s): X-ray flux in the soft (0.5–2 keV) band in 10^{-15} erg s^{-1} cm^{-2}.

Column 5 (F_h): X-ray flux in the hard (2–4.5 keV) band in 10^{-15} erg s^{-1} cm^{-2}.

Column 6 (F_{vh}): X-ray flux in the veryhard (4.5–10 keV) band in 10^{-15} erg s^{-1} cm^{-2}.

Column 7 (F_{tot}): X-ray flux in the total (0.5–10 keV) band in 10^{-15} erg s^{-1} cm^{-2}.

Column 8 (F_{vh2}): X-ray flux in the veryhard2 (4.0–7 keV) band in 10^{-15} erg s^{-1} cm^{-2}.

Column 9 (F_{tot2}): X-ray flux in the total2 (0.5–7 keV) band in 10^{-15} erg s^{-1} cm^{-2}.

Column 10 (SXDS_ID): Object name in the SXDS optical catalogue (Furusawa et al. 2008).

Columns 11 and 12 (RA_0, Dec_0): Equinox J2000.0 right ascension and declination in degrees. These coordinates correspond to the centroid in the broadband optical catalogue obtained by the SXDS team (see Sect. 2).

Columns 13 and 14 (R_c, R_c_err): R_c apparent magnitude and its error.

Columns 15 and 16 (zphot, zphot_err): Photometric redshift and its error (see Sect. 2.6).

Columns 17 and 18 (MabsB, MabsB_err): Absolute magnitude in B band and its error (see Sect. 4.1).

Columns 19 and 20 ($B-V$, $B-V$_err): Rest-frame $B-V$ colour and its error (see Sect. 4.1).

Columns 21 and 22 (X/O, X/O_err): X-ray-to-optical flux ratio, computed as the ratio of the observed X-ray flux in the 0.5–4.5 keV energy range and optical flux in R_c band, and its error.

Columns 23 and 24 (HR, HR_err): (2–4.5/0.5–2 keV) hardness ratio and its error (see Sect. 2).

Column 25 (Stellarity): SExtractor CLASS_STAR parameter Column objects assigned as compact are all objects with this parameter ≥0.9 (see Sect. 3.1).

Column 26 (Elong): Elongation parameter obtained by SExtractor (Bertin & Arnouts 1996).

Column 27 (MSB): Mean surface brightness of the source, measured by galSVM (Huertas-Company et al. 2008).

Column 28 (A): Asymmetry index measured by galSVM, defined as in Abraham et al. (1996).

Column 29 (C): Abraham concentration index, measured by galSVM and defined as the ratio between the integrated flux within certain radius defined by the normalized radius =0.3, and the total flux (Abraham et al. 1996).

Column 30 (Gini): Gini coefficient measured by galSVM and defined as in Abraham et al. (2003).

Column 31 (S): Smoothness of the source, measured by galSVM and defined as in Conselice et al. (2003).

Column 32 (M_{20}): Moment of light M_{20}, measured by galSVM and defined as in Lotz et al. (2004).

Columns 33 and 34 ($p1$, $p2$): Probability that the galaxy is early- or late-type, respectively (see Sect. 3.2).

References

Abraham, R. G., van den Bergh, S., Glazebrook, K., et al. 1996, ApJS, 107, 1
Abraham, R. G., van den Bergh, S., & Nair, P. 2003, ApJ, 588, 218
Adams, T. F. 1977, ApJS, 33, 19
Alexander, D. M., Brandt, W. N., Hornschemeier, A. E., et al. 2001, AJ, 122, 2156
Alonso-Herrero, A., Pérez-González, P. G., Rieke, G. H., et al. 2008, ApJ, 677, 127
Aretxaga, I., Hughes, D. H., Coppin, K., et al. 2007, MNRAS, 379, 1571
Baldry, I. K., Glazebrook, K., Brinkmann, J., et al. 2004, ApJ, 600, 681
Barcons, X., Carrera, F. J., Ceballos, M. T., et al. 2007, A&A, 476, 1191
Barger, A. J., Cowie, L. L., Capak, P., et al. 2003, AJ, 126, 632
Barnes J. E., & Hernquist L. 1996, ApJ, 471, 115
Bershady, M. A., Jangren, A., & Conselice, C. J. 2000, AJ, 119, 2645
Bertin, E., & Arnouts, S. 1996, A&AS, 117, 393
Blanton, M. R., & Roweis, S. 2007, AJ, 133, 734
Blanton, M. R., Dalcanton, J., Eisenstein, D., et al. 2001, AJ, 121, 2358
Bolzonella, M., Miralles, J. M., & Pelló, R. 2000, A&A, 363, 476
Brusa, M., Fiore, F., Santini, P., et al. 2009, A&A, 507, 1277
Caccianiga, A., Severgnini, P., Braito, V., et al. 2004, A&A, 416, 901
Calzetti, D., Armus, L., Bohlin, R. C., et al. 2000, ApJ, 533, 682
Cardamone, C. N., Urry, C. M., Schawinski, K., et al. 2010, ApJ, 721, L38
Cepa, J., Alfaro, E. J., Castañeda, H. O., et al. 2007, RMxAC, 29, 168
Cepa, J., Pérez-García, A. M., Bongiovanni, A., et al. 2008, A&A, 490, 1
Cepa, J., Bongiovanni, A., Pérez-García, A. M., et al. 2011, Highlights of Spanish Astrophysics VI, 167
Ciotti, L., & Ostriker, J. P. 2007, ApJ, 665, 1038
Ciotti, L., Ostriker, J. P., & Proga, D. 2009, ApJ, 699, 89
Cirasuolo, M., Magliocchetti, M., & Celotti, A. 2005, MNRAS, 357, 1267
Cisternas, M., Jahnke, K., Inskip, K. J., et al. 2011, ApJ, 726, 57
Civano, F., Mignoli, M., Comastri, A., et al. 2007, A&A, 476, 1223
Choi, Y.-Y., Woo, J.-H., & Park, C. 2009, ApJ, 699, 1679
Conselice, C. J., Bershady, M. A., Dickinson, M., & Papovich, C. 2003, AJ, 126, 1183
Cox, T. J., Jonsson, P., Somerville, R. S., Primack, J. R., & Dekel, A. 2008, MNRAS, 384, 386
Croton, D. J., Springel, V., White, S. D. M., et al. 2006, MNRAS, 365, 11
Davies, R. I., Müller Sánchez, F., Genzel, R., et al. 2007a, ApJ, 671, 1388
Davis, M., Guhathakurta, P., Konidaris, N. P., et al. 2007b, ApJ, 660, 1
Della Ceca, R., Maccacaro, T., Caccianiga, A., et al. 2004, A&A, 428, 383
Dickey, J. M., & Lockman, F. J. 1990, ARA&A, 28, 215
Di Matteo, T., Springel, V., & Hernquist, L. 2005, Nature, 433, 604
Dwelly, T., Page, M. J., Loaring, N. S., et al. 2005, MNRAS, 360, 1426
De Ruiter, H. R., Willis, A. G., & Arp, H. C. 1977, A&AS, 28, 211
Feldmann, R., Carollo, C. M., Porciani, C., et al. 2006, MNRAS, 372, 565
Fernández Lorenzo, M., Cepa, J., Bongiovanni, A., et al. 2010, A&A, 521, A27
Ferrarese, L. 2004, in Supermassive Black Holes in the Distant Universe, ed. A. Barger (Netherlands: Kluwer Academic Publishers), 1
Ferrarese, L., & Merrit, D. 2000, ApJ, 539, L9
Fiore, F., Brusa, M., Cocchia, F., et al. 2003, A&A, 409, 79
Furusawa, H., Kosugi, G., Akiyama, M., et al. 2008, ApJS, 176, 1
Gabor, J. M., Impey, C. D., Jahnke, K., et al. 2009, ApJ, 691, 705
Gebhardt, K., Bender, R., Bower, G., et al. 2000, ApJ, 539, L13
Georgakakis, A., Nandra, K., Laird, E. S., et al. 2007, ApJ, 660, L15
Georgakakis, A., Nandra, K., Yan, R., et al. 2008, MNRAS, 385, 2049
Georgakakis, A., Coil, A. L., Laird, E. S., et al. 2009, MNRAS, 397, 623
Governato, F., Brook, C. B., Brooks, A. M., et al. 2009, MNRAS, 398, 312
Graham, A. W., Erwin, P., Trujillo, I., & Caon, N. 2001a, ApJ, 563, L11
Graham, A. W., Trujillo, I., & Caon, N. 2001b, AJ, 122, 1707
Griffith, R. L., & Stern, D. 2010, AJ, 140, 533
Grogin, N. A., Conselice, C. J., Chatzichristou, E., et al. 2005, ApJ, 627, 97
Hasinger, G. 2008, A&A, 490, 905
Hasinger, G., Miyaji, T., & Schmidt, M. 2005, A&A, 441, 417
Hasinger, G., Cappelluti, N., Brunner, H., et al. 2007, ApJS, 172, 29
Heckman, T. M. 1978, PASP, 106, 113
Hewett, P. C., Warren, S. J., Leggett, S. K., & Hodgkin, S. T. 2006, MNRAS, 367, 454
Hickox, R. C., Jones, C., Forman, W. R., et al. 2009, ApJ, 696, 891
Ho, L. C., Filippenko, A. V., & Sargent, W. L. 1995, ApJS, 98, 477
Hodgkin, S. T., Irwin, M. J., Hewett, P. C., & Warren, S. J. 2009, MNRAS, 394, 675
Hopkins, P. F. 2008b, ApJS, 175, 390
Hopkins, P. F. 2012, MNRAS, 420, L8
Hopkins, P. F., & Hernquist, L. 2009, ApJ, 694, 599
Hopkins, P. F., Hernquist, L., Cox, T. J., et al. 2005a, ApJ, 630, 705
Hopkins, P. F., Hernquist, L., Martini, P., et al. 2005b, ApJ, 625, L71
Hopkins, P. F., Hernquist, L., Cox, T. J., & Kereš, Dušan, 2008a, ApJS, 175, 356
Huertas-Company, M., Rouan, D., Tasca, L., Soucail, G., & Le Fèvre, O. 2008, A&A, 478, 971
Huertas-Company, M., Tasca, L., Rouan, D., et al. 2009, A&A, 497, 743
Kauffmann, G., Heckman, T. M., Tremonti, C., et al. 2003, MNRAS, 346, 1055
Kauffmann, G., Heckman, T. M., Budavári, T., et al. 2007, ApJS, 173, 357
Kent, S. M. 1985, ApJS, 59, 115
Kormendy, J., & Kennicutt, Jr. R. C. 2004, ARA&A, 42, 603
Kormendy, J., & Richstone, D. 1995, ARA&A, 33, 581
Lara-López, M. A., Cepa, J., Castañeda, H., et al. 2010, PASP, 122, 1495
Lawrence, A., Warren, S. J., Almaini, O., et al. 2007, MNRAS, 379, 1599
Lotz, J. M., Primack, J., & Madau, P. 2004, AJ, 128, 163
Magorrian, J., Tremaine, S., Richstone, D., et al. 1998, AJ, 115, 2285
Mainieri, V., Bergeron, J., Hasinger, G., et al. 2002, A&A, 393, 425
Mainieri, V., Bongiorno, A., Merloni, A., et al. 2011, A&A, 535, A80
Marconi, A., & Hunt, L. K. 2003, ApJ, 589, L21
Mateos, S., Barcons, X., Carrera, F. J., et al. 2005, A&A, 444, 79
McLure, R. J., Dunlop, J. S., & Kukula, M. J. 2000, MNRAS, 318, 693
Melbourne, J., Phillips, A. C., Harker, J., et al. 2007, ApJ, 660, 81
Mortier, A. M. J., Serjeant, S., Dunlop, J. S., et al. 2005, MNRAS, 363, 563
Mukai, K. 1993, Legac, 3, 21
Nandra, K., Georgakakis, A., Willmer, C. N. A., et al. 2007, ApJ, 660, L11
Peng, C. J., Impey, C. D., Ho, L. C., Barton, E. J., & Rix, H.-W. 2006a, ApJ, 640, 114
Peng, C. J., Impey, C. D., Rix, H.-W., et al. 2006b, ApJ, 649, 616
Perola, G. C., Puccetti, S., Fiore, F., et al. A&A, 421, 491
Pierce, C. M., Lotz, J. M., Laird, E. S., et al. 2007, ApJ, 660, L19
Pierce, C. M., Lotz, J. M., Salim, S., et al. 2010, MNRAS, 408, 139
Polletta, M., Tajer, M., Maraschi, L., et al. 2007, ApJ, 663, 81
Pović, M., Sánchez-Portal, M., Pérez García, A. M., et al. 2009a, ApJ, 706, 810
Pović, M., Sánchez-Portal, M., Pérez García, A. M., et al. 2009b, ApJ, 702, L51
Reach, W. T., Megeath, S. T., Cohen, M., et al. 2005, PASP, 117, 978
Robertson, B., Bullock, J. S., Cox, T. J., et al. 2006, ApJ, 645, 986
Sánchez, S. F., Jahnke, K., Wisotzki, L., et al. 2004, ApJ, 614, 586
Schawinski, K., Khochfar, S., Kaviraj, S., et al. 2006, Nature, 442, 888
Schawinski, K., Virani, S., Simmons, B., et al. 2009, ApJ, 692, L19
Schawinski, K., Urry, C. M., Virani, S., et al. 2010, ApJ, 711, 284
Scoville, N., Aussel, H., Brusa, M., et al. 2007, ApJS, 172, 1
Shin, M.-S., Ostriker, J. P., & Ciotti, L. 2010, ApJ, 711, 268
Silverman, J. D., Green, P. J., Barkhouse, W. A., et al. 2005, ApJ, 618, 123
Silverman, J. D., Mainieri, V., Lehmer, B. D., et al. 2008, ApJ, 675, 1025
Simpson, C., Martínez-Sansigre, A., Rawlings, S., et al. 2006, MNRAS, 372, 741
Somerville, R. S., Hopkins, P. F., Cox, T. J., Robertson, B. E., & Hernquist, L. 2008, MNRAS, 391, 481
Springel, V., & Hernquist, L. 2005, ApJ, 622, L9
Springel, V., White, S. D. M., Jenkins, A., et al. 2005, Nature, 435, 629
Steffen, A. T., Strateva, I., Brandt, W. N., et al. 2006, AJ, 131, 2826
Strüder, L., Briel, U., Dennerl, K., et al. 2001, A&A, 365, L18
Surace, J. A., Sanders, D. B., & Evans, A. S. 2000, ApJ, 529, 170
Surace, J. A., et al. 2005, DR2 paper draft http://swire.ipac.caltech.edu/swire/astronomers/data_access.html
Sutherland, W., & Saunders, W. 1992, MNRAS, 259, 413
Tasca, L. A. M., & White, S. D. M. 2011, A&A, 530, A106
Taylor, M. B. 2005, ASPC, 347, 29
Treister, E., Virani, S., Gawiser, E., et al. 2009, ApJ, 693, 1713
Tully, R. B., Pierce, M. J., Huang, J.-S., et al. 1998, AJ, 115, 2264
Turner, M. J. L., Abbey, A., Arnaud, M., et al. 2001, A&A, 365, L27
Vapnik, V. 1995, The Nature of statistical Learning Theory (Springer-Verlag), 536
Ueda, Y., Watson, M. G., Stewart, I. M., et al. 2008, ApJS, 179, 124
Wada, K. 2004, Coevolution of Black Holes and Galaxies, 186
Warren, S. J., Hambly, N. C., Dye, S., et al. 2007, MNRAS, 375, 213
Weiner, B. J., Benjamin J., Phillips, A. C., et al. 2005, ApJ, 620, 595
Wild, V., Heckman, T., & Charlot, S. 2010, MNRAS, 405, 933
Wolf, C., Dye, S., Kleinheinrich, M., et al. 2001, A&A, 377, 442
Wolf, C., Meisenheimer, K., Kleinheinrich, M., et al. 2004, A&A, 421, 913
Wolf, C., Hildebrandt, H., Taylor, E. N., & Meisenheimer, K. 2008, A&A, 492, 933
Xue, Y. Q., Brandt, W. N., Luo, B., et al. 2010, ApJ, 720, 368
Younes, G., Porquet, D., Sabra, B., & Reeves, J. N. 2011, A&A, 530, A149